LOCALIZED SURFACE PLASMONS IN METAL NANOPARTICLES ENGINEERED BY ELECTRON BEAM LITHOGRAPHY

A THESIS SUBMITTED TO
THE GRADUATE SCHOOL OF NATURAL AND APPLIED SCIENCES
OF
MIDDLE EAST TECHNICAL UNIVERSITY

BY

URCAN GÜLER

IN PARTIAL FULFILLMENT OF THE REQUIREMENTS
FOR
THE DEGREE OF MASTER OF SCIENCE
IN
PHYSICS

SEPTEMBER 2009

Approval of the thesis:

LOCALIZED SURFACE PLASMONS IN METAL NANOPARTICLES ENGINEERED BY ELECTRON BEAM LITHOGRAPHY

submitted by **URCAN GÜLER** in partial fulfillment of the requirements for the degree of **Master of Science in Physics Department, Middle East Technical University** by,

Prof. Dr. Canan Özgen
Dean, Graduate School of **Natural and Applied Sciences** _____________

Prof. Dr. Sinan Bilikmen
Head of Department, **Physics** _____________

Prof. Dr. Raşit Turan _____________
Supervisor, **Department of Physics, METU**

Examining Committee Members:

Prof. Dr. M. Pınar Mengüç
Department of Mechanical Engineering, Özyeğin University _____________

Prof. Dr. Raşit Turan
Department of Physics, METU _____________

Prof. Dr. Şinasi Ellialtıoğlu
Department of Physics, METU _____________

Asst. Prof. Hakan Altan
Department of Physics, METU _____________

Asst. Prof. Ceyhun Bulutay
Department of Physics, Bilkent University _____________

Date: 08.09.2009

I hereby declare that all information in this document has been obtained and presented in accordance with academic rules and ethical conduct. I also declare that, as required by these rules and conduct, I have fully cited and referenced all material and results that are not original to this work.

Name, Last name : URCAN GÜLER

Signature :

ABSTRACT

LOCALIZED SURFACE PLASMONS IN METAL NANOPARTICLES ENGINEERED BY ELECTRON BEAM LITHOGRAPHY

Güler, Urcan
M.Sc., Department of Physics
Supervisor: Prof. Dr. Raşit Turan

September 2009, 96 pages

In this study, optical behavior of metal nanoparticles having dimensions smaller than the wavelength of visible light is studied experimentally and numerically. Gold (Au) and silver (Ag) nanoparticles are studied due to their superior optical properties when compared to other metals. A compact code based on Discrete Dipole Approximation (DDA) is developed to compute extinction efficiencies of nanoparticles with various different properties such as material, dimension and geometry. To obtain self consistent nanoparticle arrays with well defined geometries and dimensions, Electron Beam Lithography (EBL) technique is mainly used as the manufacturing method. Dose parameters required to produce nanoparticles with dimensions down to 50 nm over substrates with different electrical conductivities are determined. Beam current is found to affect the dose-size relation. The use of thin Au films as antistatic layer for e-beam patterning over insulating substrates is considered and production steps, involving instabilities due to contaminants introduced to the system during additional removal steps, are clarified. 4 nm thick Au layer is found to provide sufficient conductivity for e-beam patterning over insulating substrates. An optical setup capable of performing transmittance and reflectance measurements of samples having small areas patterned with EBL is designed. Sizes of the metal nanoparticles are determined by scanning electron microscope (SEM) and spectral data obtained using the optical setup is analyzed to find out the parameters affecting the localized surface plasmon resonances (LSPR). Arrays of particles with diameters between 50 – 200 nm are produced and optically analyzed. Size and shape of the nanoparticles are found to affect the resonance behavior. Furthermore, lattice constants of the particle arrays and surrounding medium are also shown to influence the reflectance spectra. Axes with different lengths in ellipsoidal nanoparticles are observed to cause distinguishable resonance peaks when illuminated with polarized light. Peak intensities obtained from both polarizations are observed to decrease under unpolarized illumination. Binary systems consisting of nanosized particles and holes provided better contrast for transmitted light.

Keywords: Metal nanoparticles, Localized Surface Plasmons, Electron Beam Lithography, Discrete Dipole Approximation.

ÖZ

ELEKTRON DEMET LİTOGRAFİSİ İLE İŞLENMİŞ METAL NANOPARÇACIKLARDA LOKALİZE YÜZEY PLAZMONLARI

Güler, Urcan
Yüksek Lisans, Fizik Bölümü
Tez Yöneticisi: Prof. Dr. Raşit Turan

Eylül 2009, 96 sayfa

Bu çalışmada ışığın görünür bölgedeki dalga boylarına görece daha küçük boyutlarda metal nanoparçacıkların optik davranışları deneysel ve nümerik olarak incelenmiştir. Diğer metallere göre daha verimli optik özellikler gösteren altın (Au) ve gümüş (Ag) ağırlıklı olarak ele alınmıştır. Belirli çift kutup yaklaşımı (DDA) esas alınarak geliştirilen yazılım yardımı ile farklı malzeme, şekil ve boyutlara sahip metal nanoparçacıkların söndürme verimlilikleri hesaplanmıştır. Kendi içerisinde tutarlı şekil ve ölçülere sahip parçacıkların üretilebilmesi için elektron demet litografisi (EBL) yöntemi kullanılmıştır. Farklı elektriksel iletkenliklere sahip alttaşların üzerine, 50 nm boyutlarına kadar küçültülmüş farklı parçacıkların işlenebilmesi için gerekli olan doz parametreleri tartışılmıştır. Demet akımının, doz ve parçacık boyutu arasındaki ilişkiye etki ettiği gözlemlenmiştir.

Yalıtkan alttaşların işlenebilmesi için gerekli olan ince Au filminin kullanılışı ve bu sırada gerekli olan ek işlemlerin getirdiği kirlenmenin gideriliş yöntemi sonuca bağlanmıştır. 4 nm kalınlığındaki Au filmlerin yalıtkan alttaşlar için gerekli olan iletkenliği sağladığı sonucuna varılmıştır. EBL yöntemi ile üretilen küçük boyutlardaki örneklerin yansıma ve geçirgenlik ölçümlerinin yapılmasını sağlayacak bir optik düzenek tasarlanarak kurulmuş ve taramalı elektron mikroskopu (SEM) ile nanoparçacıkların biçimsel özellikleri gözlemlenerek lokalize plazmon rezonanslarına etki eden mekanizmalar incelenmiştir. 50 – 200 nm boyutları arasında üretilen metal nanoparçacıkların boyutları, şekilleri, aralarındaki mesafe ve içinde bulundukları ortamın optik sabitleri rezonans davranışında etkili olmuştur. Elipsoidal parçacıklarda farklı boyutlardaki eksenlerin farklı dalga boylarında rezonansa neden oldukları polarize ışık kullanılarak gösterilmiştir. Ayrıca, polarize olmayan ışık kullanıldığında, her iki eksenden elde edilen rezonans tepelerinin zayıfladığı gözlemlenmiştir.

Anahtar Kelimeler: Metal Nanoparçacıklar, Lokalize Yüzey Plazmonları, Elektron Demet Litografisi, Belirli Çift Kutup Yaklaşımı.

to my lovely family...

ACKNOWLEDGEMENTS

I would like to thank to my supervisor Prof. Dr. Raşit Turan for providing any opportunity needed to carry out this work. His encouragement, perceptiveness and friendship played a crucial role in conclusion of this study.

I would like to thank to Seçkin Öztürk for discussions and invaluable suggestions about manufacturing process, Sedat Canlı for long hours of SEM sessions which have been the key stone of production and Adem Yenisoy for his assistance on the production of self assembled samples. Support from Mustafa Kulakçı was also indispensable for me. His endless patience gave me the chance to use thermal evaporator intensely.

Also, I want to thank to my present and former group partners Ayşe Seyhan, Umut Bostancı, İlker Doğan, Buket Kaleli, Döndü Şahin, Selçuk Yerci, Arife Gencer, İlker Yıldız, Z. Deniz Eygi, Nader A. P. Moghaddam, Dr. Ercan Yılmaz and Yücel Eke for their friendliness and endless support during this work. It was certainly didactic to be a member of such an outstanding group.

It is my pleasure to express my gratitude towards my wife Senem Güler, who has been with me for years, while building my career, without any complaint.

I would like to thank to Scientific and Technological Research Council of Turkey (TUBITAK) for partial financial support during this study.

I would also like to thank to METU Central Laboratory for enabling its wide facilities anytime needed in this work.

TABLE OF CONTENTS

CHAPTERS

LIST OF TABLES

TABLES

LIST OF FIGURES

FIGURES

LIST OF ABBREVIATIONS

LSPR	Localized Surface Plasmon Resonance
EBL	Electron Beam Lithography
SEM	Scanning Electron Microscope
DDA	Discrete Dipole Approximation
FDTD	Finite Difference Time Domain
VW	Volmer Weber
PMMA	Poly (methyl methacrylate)
ITO	Indium Tin Oxide
MIBK	Methyl isobutyl ketone
IPA	Isopropyl alcohol
DI water	Deionized water
CCD	Charge-coupled device

CHAPTER 1

INTRODUCTION

1.1 Historical Perspective

It was early in the history when man noticed the exciting optical behavior of metals, especially for particles having small sizes. Most famous examples of the use of metal nanoparticles date back to more than 1000 years before. Gold nanoparticles embedded in glass were used to generate fabulous colors on the Lycurgus cup of Byzantines like in many other windows of the ancient buildings. Of course, those products were not a result of scientific work since systematic studies do not root back to those early times. It was about 1500 years later when Michael Faraday demonstrated the optical behavior of gold nanoparticle dispersions [1]. Half a century later, Maxwell Garnet introduced the optical behavior of metal nanoparticles embedded in glass [2]. A couple of years later, it was Gustav Mie who made an attempt to solve the Maxwell equations to obtain a deeper understanding of interaction of light with metal nanoparticles having spherical symmetry which resulted in a theory being called with the name of the German physicist [3]. Being famous after the development, Mie theory is still widely used to describe the optical behavior of spherical metal nanoparticles in fields where no other complex geometries are used. Although the extraordinary properties of metallic nanostructures were discovered at the very beginning of century on paper, it could be possible to realize most of the work after the improvement of nanomanufacturing techniques. As the man made nanostructures are widely used, it has been much harder to explain the mechanisms, running through complex geometries, by use of analytical methods developed by the pioneers. Fortunately, with the help of rapidly developing computer technology, it could be possible to make use of numerical methods in efficient ways. In 1966; Yee introduced a computational algorithm, named as the Finite Difference Time Domain (FDTD) method, which is based on grid based solutions of Maxwell equations in time domain from which spectral results could also be derived with Fourier transformations [4]. Of course, it is now possible to make use of many sources devoted to the FDTD method for computational electrodynamics and softwares based on the improved technique through the history. A more specific method to explain optical behavior of small particles was suggested by Purcell and Pennypacker which was then improved by many other researchers and named as the Discrete Dipole approximation (DDA) [5]. Providing free sources and relatively faster algorithms DDA is employed widely by many research groups including us. Due to the promising results obtained from many trials to adapt the physical phenomena to technology, optics of metals having several different geometries and dimensions are now being studied by researchers all around the world. This work deals with several aspects of these systems both theoretically and experimentally.

1.2 Motivation

Although the history of plasmonics is known to be older than a century, improvement of nanomanufacturing techniques gave rise to extensive studies over the last decade. Promising results could be obtained in a wide area of applications ranging from surface enhanced raman scattering (SERS) to narrow waveguides having dimensions smaller than the wavelength of guided light [6,7]. Another field where existence of metal nanoparticles can be used to increase efficiencies is the devices based on the absorption of light. Many studies investigating the effect of metal nanoparticles on the performance enhancement of semiconductor optoelectronic devices can be found in the literature [8-12]. Enhancement effects of metallic nanoparticles were also demonstrated for dye sensitized solar cells by Hägglund et al [13]. Catchpole et al. demonstrated the adaptability of nanosized metal particles to thin film solar cells to enhance optical absorption due to increased coupling of incident light to the waveguide [14-18]. Another promising energy saving application of metal particle arrays is the enhancement of luminescence from various sources [19-21].

Studies on localized surface plasmons show that the mechanism is open to engineering due to the flexibility of optical characteristics. Tanabe studied the optical radiation efficiencies of eleven kinds of metal by use of classical electromagnetic theory [22]. Ag, Al, Au and Cu were found to have higher optical radiation efficiencies. Garcia et al. developed a self-consistent technique to predict the behavior of plasmon resonances in ternary nanocomposites as a function of wavelength in agreement with experimental data [23]. In a relatively early study, Kottman et al. showed that it is possible to predict plasmon resonances of metallic nanoparticles with different shapes by use of numerical techniques also considering the polarization of incident radiation [24].

The objective of this work is to investigate the optical behavior of metal nanoparticles produced by use of the electron beam lithography (EBL) method. Providing self consistent and well defined structures, EBL helps understanding the parameters affecting the resonance behavior of nanoparticle arrays. Since the enhancement of absorption in the host material is intended, particles having higher scattering efficiencies are considered. Silver and gold nanoparticles were chosen because of their significant optical advantages when compared to other metals. In chapter 2, basic boundary condition problems of sphere and infinite cylinder under uniform electric field are considered to gain an insight to the polarization effects leading to light scattering characteristics. Also; the dielectric functions of metals, that makes them suitable for the well known resonance conditions, were studied by use of different models emerged in the history that are found to be successful although being classical. In chapter 3, the well known exact theory of Mie is introduced since it is widely used for systems consisting of particles having spherical symmetry. In addition, to be able to model particles having relatively larger dimensions leading to multipole scattering and more complex geometries, discrete dipole approximation (DDA) method is represented and employed. Also, results for some simple configurations are considered to check the validity of the code written. Chapter 4 is devoted to the manufacturing issues and characterization techniques used in the experiments. Dose parameters used to produce metal nanoparticles with different dimensions over substrates having different electrical conductivities are discussed. Optical setups designed to examine the transmittance and reflectance properties of nanoparticle arrays are presented. Also, a short introduction to the self assembly growth of metals is given due to the importance of this method. Being an easy and rapid method, also applicable to large areas, self assembled metal nanoparticles can be considered as one of the promising manufacturing methods for mass production. In chapter 5, optical data obtained from several different arrays of metal nanoparticles are presented and compared with the corresponding results for structures modeled with DDA simulations. Finally, chapter 6 presents conclusions to the work conducted in this study.

CHAPTER 2

LOCALIZED SURFACE PLASMON RESONANCE

Surface plasmons are basically called as the localized surface plasmons (LSP) when they are confined in metal nanostructures and considered to be promising for applications in a variety of fields [25-28]. For the case of nanoparticles having dimensions small enough when compared to the wavelength of the incident light; i.e. $< \lambda/_{10}$, exact solutions can be obtained for some simple geometries. Although many numerical techniques are available and widely used to explore interaction of light with small particles having any geometry and size, solving Laplace equation for a particle in a uniform electric field is beneficial to gain insight of the plasmonic resonances.

2.1 Boundary Condition Problems

Use of boundary conditions to obtain exact solutions to Laplace equation for simple geometries of nanoparticles is of great importance to gain insight to the mechanisms of Plasmon resonances. In this section, elementary problems of sphere and infinite cylinder in uniform electric field will be discussed.

2.1.1 Sphere in a uniform Electric Field

Starting from the simplest case, one should consider a homogeneous, isotropic sphere with radius R located in a uniform electric field [29]. Similarly, the surrounding medium is also assumed to be isotropic with an additional restriction of negligible absorption. Since the case is in the quasistatic limit, that is, the dimensions of the sphere is very small when compared to the wavelength of illumination, phase retardation along the particle volume due to time harmonically varying field of incident light is expected to be negligible, letting us to first solve the problem for static uniform field and then add the harmonic oscillation to the solutions [30].

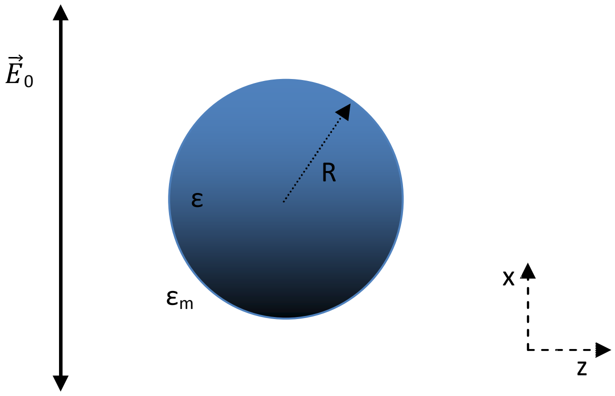

Figure 2.1: Sphere in uniform electric field.

Figure 2.1 illustrates the stated problem for an incident light propagating in z-direction with electric field polarization in x-direction where ε and ε_m are the dielectric functions of the sphere and medium, respectively. Considering a neutral sphere, the problem is simply the Laplace equation, $\nabla^2\Phi = 0$, which will lead us to the solution for the potential around the sphere. Expressing the Laplace equation in spherical coordinates to alter the problem,

$$\frac{1}{r^2 sin\theta}\left[sin\theta\frac{\partial}{\partial r}\left(r^2\frac{\partial}{\partial r}\right)+\frac{\partial}{\partial\theta}\left(sin\theta\frac{\partial}{\partial\theta}\right)+\frac{1}{sin\theta}\frac{\partial^2}{\partial\varphi^2}\right]\Phi(r,\theta,\varphi)=0 \qquad (2.1)$$

the general solutions are known to be,

$$\Phi\ (r,\theta,\varphi) = \sum_{l,m} b_{l,m} \cdot \begin{Bmatrix} r^l \\ r^{-l-1} \end{Bmatrix} \begin{Bmatrix} P_m^l\ (\cos\theta) \\ Q_m^l\ (\cos\theta) \end{Bmatrix} \begin{Bmatrix} e^{im\varphi} \\ e^{-im\varphi} \end{Bmatrix}\ , \tag{2.2}$$

where $P_m^l\ (\cos\theta)$ and $Q_m^l\ (\cos\theta)$ are the associated Legendre functions and the Legendre functions of the second kind, respectively. Obviously, to obtain the solution to the specific problem, one should consider the boundary conditions that are appropriate to the physical conditions. Since it is necessary to have finite potential at the origin, the equation (2.2) can be divided in to two separate field expressions representing the potential inside and outside the sphere,

$$\Phi_{in}\,(r,\theta) = \sum_{l=0}^{\infty} A_l\ r^l P_l(\cos\theta) \tag{2.3a}$$

$$\Phi_{out}\,(r,\theta) = \sum_{l=0}^{\infty} \left[B_l r^l + C_l r^{-(l+1)}\right]\ P_l(\cos\theta)\ . \tag{2.3b}$$

Since the applied field is given to be uniform for the entire space of the problem, potential should converge to, $\Phi_{out} = -\ E_0\, r \cos\theta$, at $r = \infty$; leading to

$$B_l = \begin{cases} -E_0, & l = 1 \\ 0, & l \neq 1 \end{cases}\ . \tag{2.4}$$

Absence of charge on the sphere results in the boundary conditions at $r = a$,

$$\frac{-1}{a}\frac{\partial \Phi_{in}}{\partial \theta}\bigg|_{r=a} = \frac{-1}{a}\frac{\partial \Phi_{out}}{\partial \theta}\bigg|_{r=a} \tag{2.5a}$$

$$-\varepsilon\frac{\partial \Phi_{in}}{\partial r}\bigg|_{r=a} = -\varepsilon_m\frac{\partial \Phi_{out}}{\partial r}\bigg|_{r=a} \tag{2.5b}$$

By use of the boundary conditions expressed above, one can find out the coefficients A_l and C_l as,

$$A_l = \begin{cases} -E_0\left(\frac{3\varepsilon_m}{\varepsilon+2\varepsilon_m}\right), & l = 1 \\ 0\quad , & l \neq 1 \end{cases} \tag{2.6a}$$

$$C_l = \begin{cases} -a^3 E_0 \left(\frac{\varepsilon - \varepsilon_m}{\varepsilon + 2\varepsilon_m}\right), & l = 1 \\ 0 \ , & l \neq 1 \end{cases} \tag{2.6b}$$

Inserting the coefficients A_l, B_l and C_l in to equations (2.3a) and (2.3b), potential inside and outside the sphere is,

$$\Phi_{in} = -\left(\frac{3\varepsilon_m}{\varepsilon + 2\varepsilon_m}\right) E_0 r \cos\theta \tag{2.7a}$$

$$\Phi_{out} = -E_0 r \cos\theta + \left(\frac{\varepsilon - \varepsilon_m}{\varepsilon + 2\varepsilon_m}\right) E_0 a^3 \frac{\cos\theta}{r^2}\,. \tag{2.7b}$$

Field outside the sphere is obviously a superposition of the applied field given at the very beginning of the problem and the field scattered by the sphere. One can easily notice the similarity between an ideal dipole potential and the second term given in equation (2.7b). It is possible to express the field outside the sphere as

$$\Phi_{out} = -E_0 r \cos\theta + \frac{\boldsymbol{p}.\boldsymbol{r}}{4\pi\varepsilon_0\varepsilon_m r^3} \tag{2.8}$$

where the dipole has a dipole moment

$$\boldsymbol{p} = 4\pi\varepsilon_0\varepsilon_m a^3 \frac{\varepsilon - \varepsilon_m}{\varepsilon + 2\varepsilon_m} \boldsymbol{E}_0. \tag{2.9}$$

Polarizability, α, of the sphere is then,

$$\alpha = 4\pi a^3 \frac{\varepsilon - \varepsilon_m}{\varepsilon + 2\varepsilon_m}\ . \tag{2.10}$$

Equation (2.10) can be interpreted as the conclusion of the problem of a sphere located in uniform static electric field. It is clear that polarizability of the sphere can be enhanced by a choice of the material for both the sphere and the medium. As the denominator of the equation (2.10) approaches zero, a resonance will occur and the field around the sphere will be enhanced tremendously. As it is already mentioned above, choice of the material for both the sphere and the surrounding medium plays a crucial role on the resonance condition. In the stated problem, medium where the sphere is located was considered to be non-absorbing. One can consider a very slowly varying positive dielectric function for the medium in the visible region since it is the case for many practical materials. Then, the material of the sphere should be chosen such that the dielectric function is a strong dependant of the frequency of incident light. As a result, it can be possible to have a resonance condition for some particular frequencies in the visible region. It should also be noted that the sphere should have negative dielectric constants for the regions where resonance is expected. Metals are known to have negative and strongly varying dielectric constants with the frequency of illumination which makes them suitable to be used for plasmonics. Later in this study, derivation of dielectric constants of metals will also be given. One can also conclude from equation (2.10) that the complex part of dielectric constant of the metal will reduce the enhancement in the field due to non-vanishing denominator in the polarizability term.

2.1.2 Infinite Cylinder in a uniform Electric Field

Another geometry that allows the exact solution of Laplace equation is the infinite cylinder. Figure 2.2 illustrates the problem of an infinite cylinder located in uniform static electric field. Such a configuration is suitable to help us understand, in the quasistatic limit, the field distribution around a nanowire having symmetry axis in z-direction where the incident light propagates. Light is chosen to be

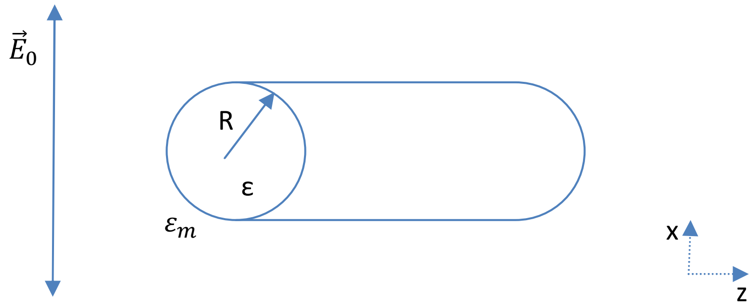

Figure 2.2: Infinite cylinder in uniform electric field.

polarized in x-direction. Once again, we will be solving the Laplace equation but this time in cylindrical coordinates. Starting point is then,

$$\frac{1}{r}\frac{\partial}{\partial r}\left(r\frac{\partial \Phi}{\partial r}\right)+\frac{1}{r^2}\left(\frac{\partial^2 \Phi}{\partial^2 \varphi^2}\right)=0\,. \tag{2.11}$$

By use of separation of variables, it is possible to obtain two simple differential equations which will lead us to angular and radial solutions. The general expressions to the field inside and outside the infinite cylinder are,

$$\Phi_{in}=\sum_{n=1}^{\infty}\alpha_n\, r^n \cos n\varphi \tag{2.12a}$$

$$\Phi_{out}=-E_0 r\cos\varphi+\sum_{n=1}^{\infty}\beta_n\, r^{-n}\cos(n\varphi) \tag{2.12b}$$

where constants are to be determined by use of the cylindrical analogue of the boundary conditions given in equations (2.5a) and (2.5b). Since there is no excess charge on the infinite cylinder, continuity of the tangential electric field component and normal electric displacement component sets the coefficients to be,

$$\alpha_1=-E_0\frac{2\varepsilon}{\varepsilon+\varepsilon_m} \tag{2.13a}$$

$$\beta_1=a^2E_0\frac{\varepsilon_m-\varepsilon}{\varepsilon+\varepsilon_m} \tag{2.13b}$$

Once the coefficients of the general solution for the field distribution are known, it can be noticed that the resonance behavior for the case of an infinite cylinder is very similar to the case of the sphere. However, this time, the condition for divergence is, $Re\big(\varepsilon(\omega)\big)=-\varepsilon_m$, differing from the case considered above. Another difference between those two cases is the field decay rate. Considering the equations (2.7b) and (2.12b), one can obviously see that the field around the nanoparticle decays within a shorter distance in the case of sphere when compared to the infinite cylinder.

So far, the elementary problem of an object located in a uniform static electric field was examined by use of Laplace equation and it was seen that it is possible to describe the resonance conditions for localized surface plasmons for nanoparticles having sizes in the quasistatic limit. Although the method is only applicable to a few simple geometries, it always helps understanding the parameters affecting the interaction of light with the particle. Dielectric constants of both the particle itself and the surrounding medium were found to play a crucial role on the results. At this point, it should be mentioned that what makes plasmonics a promising tool for sensing applications is the dependence of resonance wavelength to the dielectric constant of the host material that changes when additional molecules are attached to the system.

It was also seen that the shape of the particle makes observable changes on the resonance wavelength, bringing another degree of freedom to tune the spectral region of interest. For both cases discussed in this section, field inside the objects were found to be constant reminding us that the dimensions we are considering are smaller than the skin depth of metals. Another result of the small dimensions discussed here is the dipole term emerged in the field distribution. If larger dimensions are to be considered, multipole terms should also be included in the solutions.

2.2 The Dielectric Function

In the preceding section, solutions to the boundary condition problems for simple geometries pointed out that dielectric constants of both the particle itself and the host medium plays a crucial role on the resonance condition. Dielectric constants of solids are well studied due to their dominance on the optical properties of materials [31]. In this section, two models explaining the optical properties based on a classical approach will be reviewed to obtain the dielectric constants of metals.

2.2.1 Drude Model

For most cases metals can be approximated as the collection of free, independent electrons that do not interact with each other to describe the physical behavior [32]. Starting from this approximation one can write down the equation of motion for electrons in a metal under a time harmonic force with a frequency, ω, and electric field amplitude E_0,

$$m_e \frac{\partial^2 \boldsymbol{x}}{\partial t^2} + m_e \Gamma \frac{\partial x}{\partial t} = e\boldsymbol{E}_0 e^{-i\omega t} \tag{2.14}$$

where m_e and e are the effective mass and the charge of a free electron. Γ stands for the damping constant due to collisions of electrons with immobile positive ions and can be represented as, $\Gamma = \frac{1}{\tau} = \frac{v_f}{l}$. Damping constant is considered to be inversely proportional to the average time between collisions, τ, which in turn is proportional to the Fermi Velocity divided by the mean free path of the electrons inside the metal. Figure 2.3 illustrates the motion of electrons in a Drude material under external electric field.

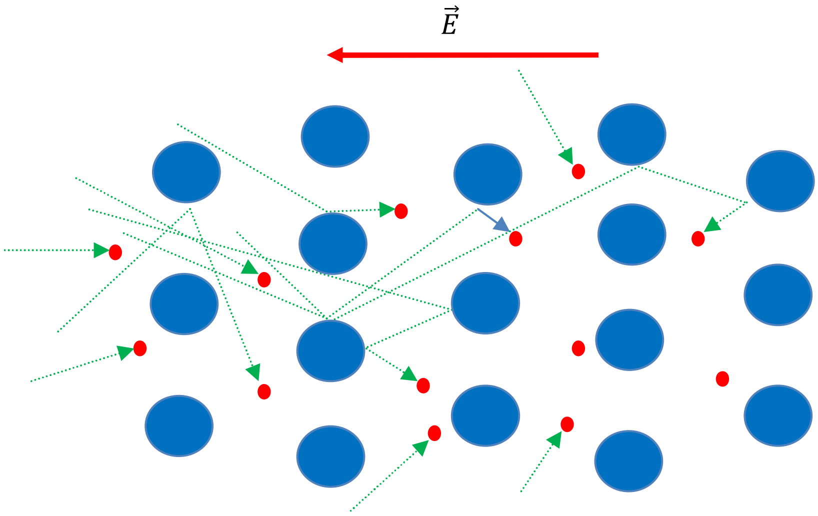

Figure 2.3: Illustration of free electrons bouncing between impurities and phonons in a Drude material under an external electric field.

Due to the time harmonic field applied to the material, one can expect a time harmonic solution for the displacement of electrons.

$$\boldsymbol{x}(t) = \boldsymbol{x}_0 e^{i\omega t} \qquad (2.15)$$

where the amplitude of the oscillation, x_0, can easily be found from equation (2.14) to be,

$$\boldsymbol{x}_0 = \frac{-e}{m_e} \frac{1}{\omega^2 + i\Gamma\omega} \boldsymbol{E}_0 \, . \qquad (2.16)$$

By use of the displacement given in equation (2.16), it is possible to express the polarization, $\boldsymbol{P} = N\boldsymbol{p} = Ne\boldsymbol{x}$, as;

$$\boldsymbol{P} = \frac{{\omega_p}^2}{\omega^2 + i\Gamma\omega} \varepsilon_0 \boldsymbol{E} \qquad (2.17)$$

where ω_p is the plasma frequency of the metal being considered,

$$\omega_p = \sqrt{{Ne^2}/{m\varepsilon_0}} \cdot \qquad (2.18)$$

Using the well known expression for polarization,

$$\boldsymbol{P} = \varepsilon_0 \chi_e \boldsymbol{E} \qquad (2.19)$$

with the susceptibility that can also be given as, $\chi_e(\omega) = \varepsilon(\omega) - 1$, one can obtain the dielectric function of a metal approximated as a collection of free electrons from equation (2.17) as,

$$\varepsilon_{Drude}(\omega) = 1 - \frac{{\omega_p}^2}{\omega^2 + i\Gamma\omega} \, . \qquad (2.20)$$

Dielectric function is most commonly separated to real and imaginary parts in the literature since both have significant effects on the optical behavior of the material. The real and imaginary parts of the dielectric function of a metal derived from the Drude model is then,

$$\varepsilon' = 1 - \frac{\omega_p{}^2}{\omega^2 + \Gamma^2} \tag{2.21a}$$

$$\varepsilon'' = \frac{\Gamma \omega_p{}^2}{\omega(\omega^2 + \Gamma^2)} \ . \tag{2.21b}$$

2.2.2 Lorentz Model

Considering free electrons in the preceding section, a satisfactory result for metals in low frequency regime was obtained. However, for the case of real metals, Drude model fails to describe the optical behavior at high frequencies due to interband transitions that are not taken into account in the calculations. At this point Lorentz model of bound electrons helps solving the deviation problem of the calculated dielectric constants at higher frequencies from the experimental results. Simply considering a system consisting of electrons and ions, one can describe the physics of a bound electron with masses bound to a spring with a spring constant, *k*. Figure 2.4 illustrates the simple harmonic oscillator approach to the electron-ion system used in the Lorentz model.

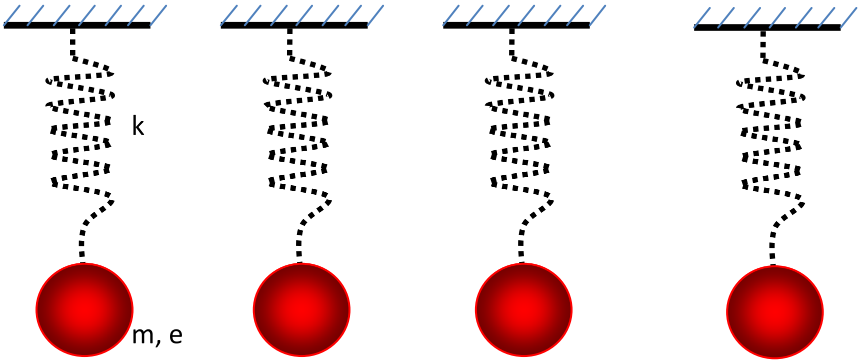

Figure 2.4: Illustration of the simple harmonic oscillators used in the Lorentz model to describe matter.

Modifying the equation of motion for free electron given in equation (2.14) with an additional term, one can obtain a more efficient picture of the system,

$$m\frac{\partial^2 \boldsymbol{x}}{\partial t^2} + m\gamma\frac{\partial x}{\partial t} + k\boldsymbol{x} = e\boldsymbol{E}_0 e^{-i\omega t} \qquad (2.22)$$

where m is the effective mass of a bound electron, γ is the damping constant representing the radiative damping and k is the spring constant of the system keeping electron bounded. Proceeding very similar to the Drude model equation of motion, one can obtain the dielectric function of a system consisting of bound electrons,

$$\varepsilon(\omega) = 1 + \frac{{\omega_p}^2}{{\omega_0}^2 - \omega^2 - i\gamma\omega} \qquad (2.23)$$

with real and imaginary parts

$$\varepsilon' = 1 + \frac{{\omega_p}^2({\omega_0}^2 - \omega^2)}{({\omega_0}^2 - \omega^2)^2 + \gamma^2\omega^2} \qquad (2.24a)$$

$$\varepsilon'' = \frac{{\omega_p}^2\gamma\omega}{({\omega_0}^2 - \omega^2)^2 + \gamma^2\omega^2} \qquad (2.24b)$$

where ω_o is the undamped angular frequency of the simple harmonic oscillator, $\omega_0 = \sqrt{k/m}$.

Equations (2.21) and (2.24) give the dielectric constant for materials consisting of only free electrons and only bound electrons, respectively. A very straightforward and accurate approximation will be considered within this chapter later. However, now some comments on the results obtained should be done. In both two expressions of dielectric constant, the damping term exists which includes the mean free path of an electron through the material. For the case of metals, mean free path of free electrons are known to be on the order of tens of nanometers. When the size of the nanoparticles are comparable with the path that free electrons travel between successive collisions, the boundaries of the particle would be another limitation on the electron motion. Although the damping constant appears in both two configurations of free and bound electrons, the size effect will be dominant only for the former case. The modified damping constant is then,

$$\gamma_{modified} = \gamma_{bulk} + \frac{v_f}{l} \tag{2.25}$$

where γ_{bulk} is the damping constant for bulk material, v_f is the Fermi velocity and l is the effective mean free path due to the boundaries of the nanoparticle. Although the size effect can be observed for particles having sizes up to hundreds of nanometers, it becomes dominant for particle sizes of 20-30 nm. Since sizes down to 50 nm will be studied in this work, we will not be concerning about size effects on the resonance condition. Another point that should be clarified is the negative real part of the dielectric constant obtained in the Drude model. As it is clear from the relation between the dielectric constant and the refractive index, such a negative value for the dielectric constant will result in an imaginary refractive index which will, in turn, increase the rate of absorption tremendously. This is a well known optical behavior of metals. Fortunately, dimensions we will be considering are on the order of nanometers, as indicated above, being shorter than the skin depth of metals.

2.2.3 Lorentz- Drude Model

Two models discussed in the preceding sections are satisfactory in terms of explaining the optical behavior of systems consisting of free and bound electrons separately. However, in real metals, contributions from both two systems are expected. Fortunately, simply adding the dielectric terms from those two models gives accurate results. Thus the dielectric constant can be expressed as,

$$\varepsilon(\omega) = \varepsilon_f(\omega) + \varepsilon_b(\omega) \tag{2.26}$$

where '*f*' and 'b' denotes the free electron and bound electron contribution, respectively.

As a final note about the dielectric constant, it is also possible to consider multiple energy levels for bound electrons by use of multiple oscillator models which are modifications of the approach discussed above in this chapter. With such a modification, one can get more accurate results for higher frequencies where those higher energy oscillators will be dominant in the system. One can say that, the more number of oscillators are included in the theory, the more accurate results can be obtained. Considering the multiple oscillator model, the dielectric function for the bound electrons can be modified from equation (2.23) to,

$$\varepsilon(\omega) = 1 + \sum_j \frac{{\omega_{pj}}^2}{{\omega_j}^2 - \omega^2 - i\gamma_j\omega} \tag{2.27}$$

where ω_j and γ_j are the characteristic oscillation frequency and damping constant of each individual oscillator. Figure 2.5 gives the dielectric function data for gold and silver calculated with multiple oscillator model which are in agreement with the experimental values given in the study of Johnson and Christy [33].

Considering the dielectric constant data for gold and silver given in figure 2.5, one can see that the requirement of negative real part of dielectric constant is met by both metals in the visible and near infrared region where plasmonic behavior are widely studied and found to be promising. It is also observed from the results that the plasma frequency, ω_p, has red shifted in both materials due to the contributions from d-band electrons which become polarized under external electric field. Due to the polarization of those d-electrons, restoring force is reduced which results in smaller ‘natural frequencies’ of the system. Degradation of the resonance due to the imaginary part of the dielectric constant was discussed in section 2.1.1. With the data provided in the figure below, one can see that both gold and silver have nonzero imaginary part in their dielectric constant throughout the visible region and the amplitude increases in the near infrared bringing reduction in the performance. Comparing the constants of two metals, it can be concluded that silver has better optical performance which is also a well known fact.

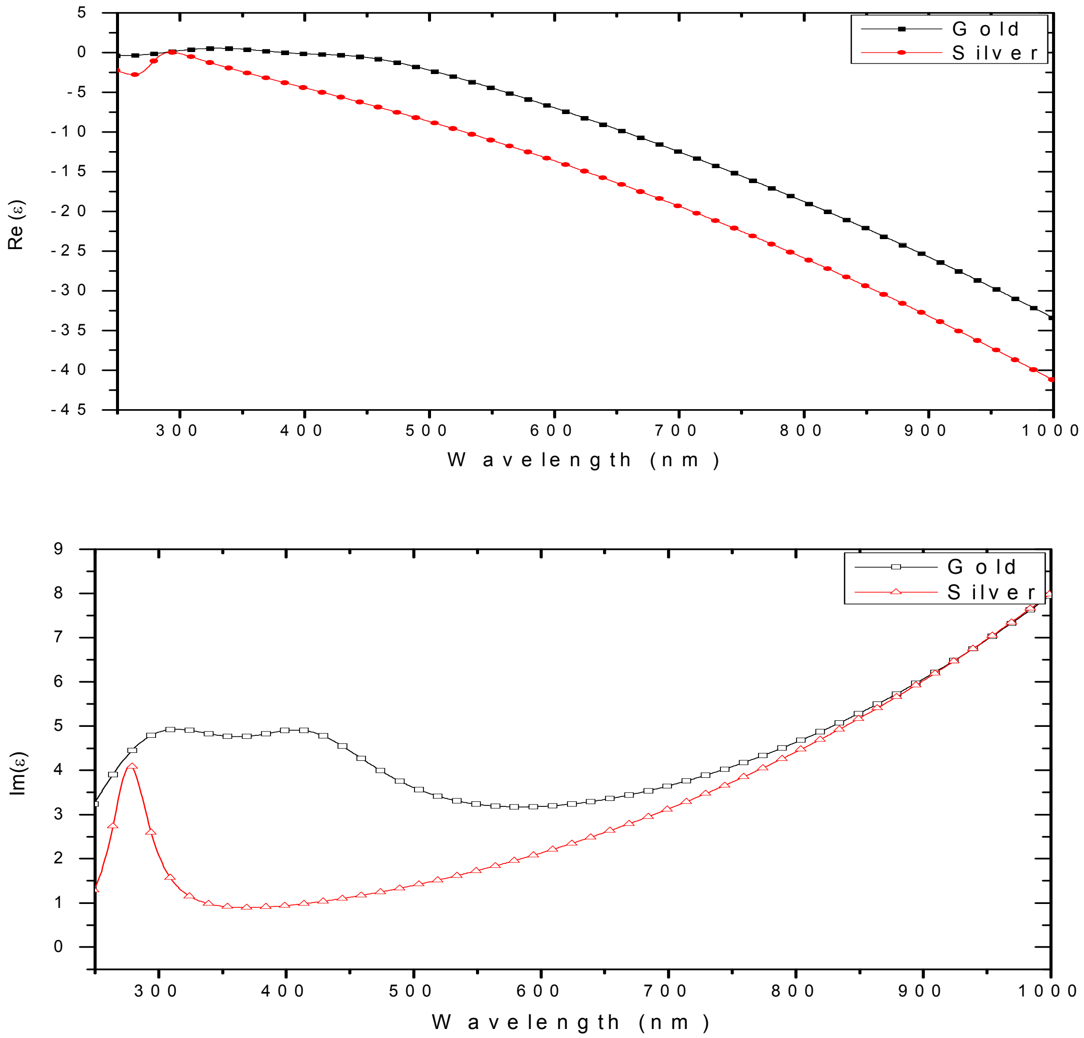

Figure 2.5: Dielectric functions of Gold and Silver versus wavelength in the visible and near-infrared region calculated with multiple oscillator model.

To study how light interacts with the particles, well known parameters such as the absorption, scattering and extinction cross sections can be used. The 'ability' of a particle to absorb, or dissipate, the incident light is given by the absorption cross section which is defined as,

$$C_{abs} = \frac{k}{\varepsilon_0} Im[\alpha(\omega)] \tag{2.28}$$

where k is the wavevector of incident light in the surrounding medium and $\alpha(\omega)$ is the polarizability of the particle. Similarly the 'ability' of the particle to re-radiate as a response to the incident light is given by the scattering cross section,

$$C_{sca} = \frac{k^4}{6\pi{\varepsilon_0}^2}|\alpha(\omega)|^2 \,. \tag{2.29}$$

The dependence of the cross sections on the polarizability of the particle is obvious from the definitions. Remembering the equation (2.10), one can notice the dependence of the cross sections to the particle size also. As the size of the particle increases, one should expect the scattering from the particle to be higher and higher as compared to the absorption. Figure 2.6 gives the comparison of absorption and scattering efficiencies of silver nanoparticles having increasing radii located in vacuum.

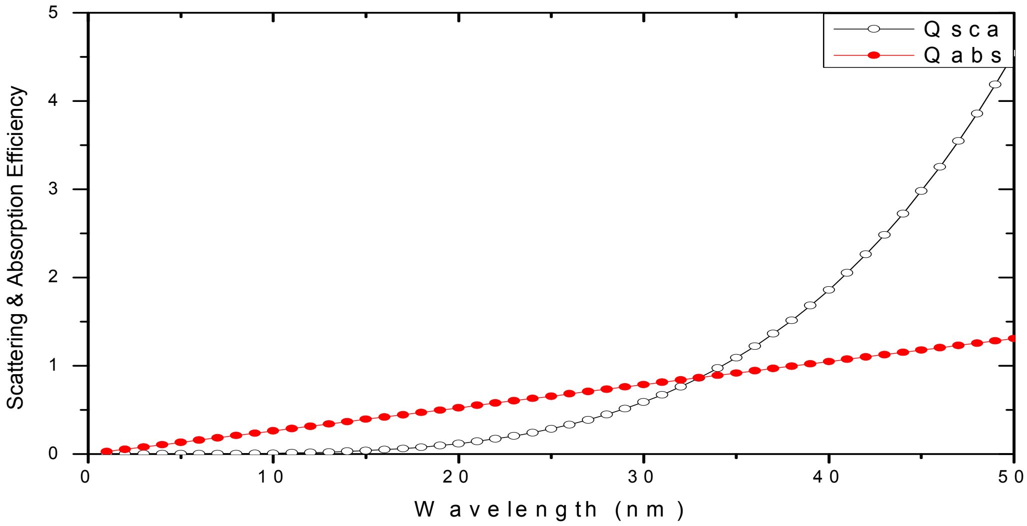

Figure 2.6: Absorption and scattering efficiencies of silver nanoparticles with increasing radii.

For the case of silver nanospheres, scattering from the nanoparticle becomes dominant for sizes larger than about 60 nm of diameter at resonance frequencies. For applications aiming to increase the light interaction with the host medium rather than the particle itself, one should make use of particles having sizes larger than some threshold value. Extinction cross section is the third parameter that needs to be used to explain the optical behavior of particles. Being the sum of absorption and scattering cross sections, extinction cross section of a particle gives the information about the total interaction of particle with the incident radiation. In mathematical terms, extinction cross section of a particle is defined as,

$$C_{ext} \equiv C_{sca} + C_{abs} \tag{2.30}$$

Having obtained the expressions to the cross sections from the quasistatic approximation and the dielectric functions of gold and silver from the multiple oscillator model, we can now examine the resonance conditions for particles small when compared to the wavelength of incident light. Figure 2.7 gives the scattering cross section normalized with the radius of the particle for both gold and silver located in vacuum.

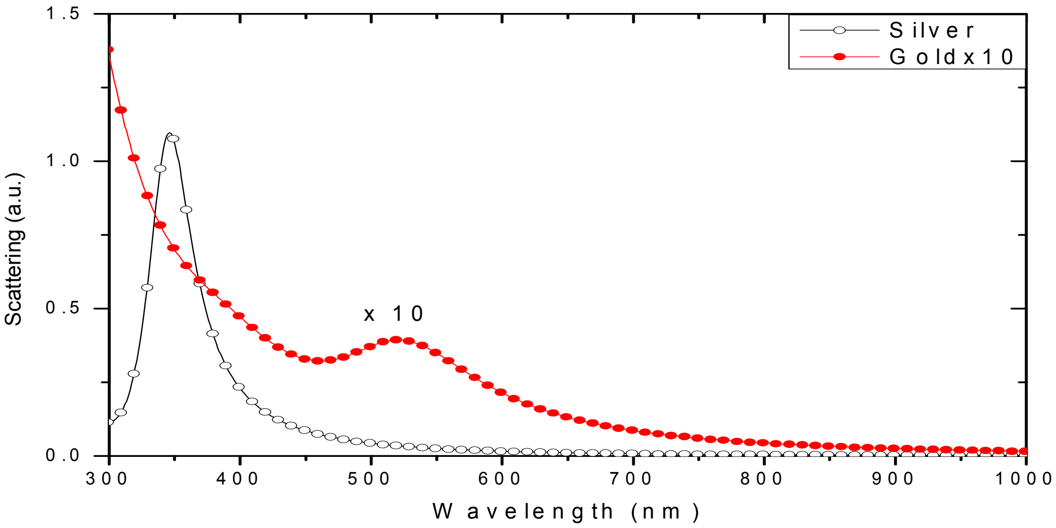

Figure 2.7: Scattering cross section normalized with the radius of the spheres for silver and gold located in vacuum.

Having the dipole terms only, figure 2.7 gives the resonance wavelengths where the interaction of light with the particle is stronger, for particles in the quasistatic limit. For more accurate results one should take the quadrupole terms into consideration. In the following chapters, we will be discussing methods allowing us to obtain more realistic results. Note that data for the gold nanoparticle is multiplied ten times to make it distinguishable, which verifies the fact that the scattering performance of gold is weaker when compared to silver due to the larger imaginary part of the dielectric constant around the resonance region.

CHAPTER 3

MODELING LSPR

So far, boundary condition problem for simple shapes were considered to explore the interaction of light with small particles due to its pedagogical way. However, as already stated in the previous chapter, it is mostly tortuous or even impossible to get exact solutions to the interaction of light with particles having widely used geometries. Mie theory, being an analytical way and only applicable to limited number of cases, is still found to be successful and used for many applications [34]. However, due to the complexity of the solutions for most geometries, some approximations are needed to predict the behavior of particles under illumination [35-37]. Numerical methods such as finite difference time domain (FDTD) method, finite element method (FEM) and discrete dipole approximation (DDA) are widely used to discover the plasmonic resonances within the framework of this approach. In this chapter, Mie theory will be reviewed with a historical perspective, and then, discrete dipole approximation will be discussed as a solution to the problems that have been considered in this work experimentally.

3.1 Mie Theory

Interaction of light with particles having sizes even in the order of wavelength was explained a century ago, in 1908, by German physicist Gustav Mie. The famous solution of Mie to the Maxwell equations is well known as the Mie Theory. The idea is simply to express a linearly polarized light, incident to a sphere, in an infinite series of vector spherical harmonics. Since it is outside the scope of this study and available in textbooks that are well known in the community [38], we will proceed with the spherical harmonic expansions of incident electric and magnetic fields,

$$\boldsymbol{E}_i = E_0 \sum_{n=1}^{\infty} i^n \frac{2n+1}{n(n+1)} \left(\boldsymbol{M}_{o1n}^{(1)} - i\boldsymbol{N}_{e1n}^{(1)} \right) \tag{3.1a}$$

$$\boldsymbol{H}_i = \frac{-k}{\omega\mu} E_0 \sum_{n=1}^{\infty} i^n \frac{2n+1}{n(n+1)} \left(\boldsymbol{M}_{e1n}^{(1)} + i\boldsymbol{N}_{o1n}^{(1)} \right) \tag{3.1b}$$

where $\boldsymbol{M}_{o1n}$, $\boldsymbol{M}_{e1n}$, $\boldsymbol{N}_{o1n}$ and $\boldsymbol{N}_{e1n}$ are the vector spherical harmonics derived from the wavefunctions, ψ_{emn} and ψ_{omn}, satisfying the scalar wave equation in spherical coordinates,

$$\psi_{emn} = \cos(m\varphi) P_n^m (\cos\theta) z_n(kr) \tag{3.2a}$$

$$\psi_{omn} = \sin(m\varphi) P_n^m (\cos\theta) z_n(kr). \tag{3.2b}$$

where z_n represents the applicable type of spherical Bessel functions. Using the boundary conditions in a very similar way to the quasistatic approximation considered in the previous chapter, one can also find the necessary expressions of the scattered field, E_s, and the field inside the sphere, E_1. Remembering that the tangential components of E and H are continuous at the boundary between the sphere and the surrounding medium, that is,

$$(E_i + E_s - E_1) \times \hat{e}_r = (H_i + H_s - H_1) \times \hat{e}_r = 0 \tag{3.3}$$

and discarding the diverging terms at the origin, one can find out that the fields inside the sphere are,

$$E_1 = \sum_{n=1}^{\infty} \frac{i^n E_0(2n+1)}{n(n+1)} \left(c_n \boldsymbol{M}_{o1n}^{(1)} - i d_n \boldsymbol{N}_{e1n}^{(1)} \right) \tag{3.4a}$$

$$H_1 = \frac{-k_1}{\omega \mu_1} \sum_{n=1}^{\infty} \frac{i^n E_0(2n+1)}{n(n+1)} \left(d_n \boldsymbol{M}_{e1n}^{(1)} + i c_n \boldsymbol{N}_{o1n}^{(1)} \right) \tag{3.4b}$$

The scattered field can also be found by use of the boundary conditions given by equation (3.3),

$$E_s = \sum_{n=1}^{\infty} \frac{i^n E_0(2n+1)}{n(n+1)} \left(i a_n \boldsymbol{N}_{e1n}^{(3)} - b_n \boldsymbol{M}_{o1n}^{(3)} \right) \tag{3.5a}$$

$$H_s = \frac{k}{\omega m} \sum_{n=1}^{\infty} \frac{i^n E_0(2n+1)}{n(n+1)} \left(i b_n \boldsymbol{N}_{o1n}^{(3)} + a_n \boldsymbol{M}_{e1n}^{(3)} \right) \tag{3.5b}$$

It should be noted at this point that the superscripts *(1)* and *(3)* given to the vector spherical harmonics indicate the type of the spherical Bessel functions included.

Having the expressions for the scattered field and the field inside the sphere, we are left to find the coefficient appeared in the solutions given by equations (3.4) and (3.5). By use of the boundary conditions given in equation (3.3) and some mathematical relations which can be found in textbooks, one can find out the desired coefficients as,

$$a_n = \frac{m^2 j_n(mx)[x j_n(x)]' - j_n(x)[mx j_n(mx)]'}{m^2 j_n(mx)\left[x h_n^{(1)}(x)\right]' - h_n^{(1)}(x)[mx j_n(mx)]'} \tag{3.6a}$$

$$b_n = \frac{j_n(mx)[x j_n(x)]' - j_n(x)[mx j_n(mx)]'}{j_n(mx)\left[x h_n^{(1)}(x)\right]' - h_n^{(1)}(x)[mx j_n(mx)]'} \tag{3.6b}$$

$$c_n = \frac{j_n(x)\left[x h_n^{(1)}(x)\right]' - h_n^{(1)}(x)[x j_n(x)]'}{j_n(mx)\left[x h_n^{(1)}(x)\right]' - h_n^{(1)}(x)[mx j_n(mx)]'} \tag{3.6c}$$

$$d_n = \frac{m j_n(x)\left[x h_n^{(1)}(x)\right]' - m h_n^{(1)}(x)[x j_n(x)]'}{m^2 j_n(mx)\left[x h_n^{(1)}(x)\right]' - h_n^{(1)}(x)[mx j_n(mx)]'} \tag{3.6d}$$

where a_n and b_n are the coefficients for the scattered field and c_n and d_n are the coefficients for the field inside the sphere. Terms x and m appearing in equations (3.6) are the size parameter, $x = 2\pi R/\lambda,$ and the relative refractive index, $m = n_s - n_m$, of the sphere, respectively.

We are now at the step of defining the optical cross sections of the spherical particle. The absorption, scattering and extinction cross sections; which are very important for describing the optical behavior of an object; can then be given as,

$$C_{sca} = \frac{2\pi}{k^2}\sum_{n=1}^{\infty}(2n+1)\left(|a|^2 + |b|^2\right) \tag{3.7a}$$

$$C_{ext} = \frac{2\pi}{k^2}\sum_{n=1}^{\infty}(2n+1)\, Re\{a_n + b_n\} \tag{3.7b}$$

$$C_{abs} = C_{ext} - C_{sca} \tag{3.7c}$$

3.2 Discrete Dipole Approximation

Although exact solutions to the problem provide a deep understanding about the physical background, numerical methods and approximations have an indispensable role on the discussion of complex geometries that are much more appropriate to nature. Presented by Purcell and Pennypacker, discrete dipole approximation (DDA) provided an efficient way of examining the interaction of light by particles with arbitrary shape and size. The method is simply to consider an object as a collection of cubically ordered polarizable elements whose polarizabilities are defined with the help of the dielectric function of the object material. In the case of this study, those objects are to be metal nanoparticles having any geometry with sizes comparable to the wavelength of illumination. DDA method was then improved in advance by Draine and Flatau to describe the optical behavior of interstellar particles [39,40]. As the field of plasmonics became much more popular with the development of nanomanufacturing methods allowing the realization of theoretical works, quest of new methods to model more realistic cases made DDA one of the most popular technique. Due to its relative easiness and applicability, DDA will be used in this work to model the systems examined experimentally.

One of the advantages of DDA is the availability of free codes developed in different environments such as DDSCAT and ADDA. However, in this work, we will be considering our own code developed by the guidance of significant work of Draine et. al. To make a short review of the idea behind the DDA, one should first consider a particle consisting of *N* polarizable elements ordered in a cubic lattice whose dipole emission affects the other *N-1* elements allowing the influences of size and shape of the particle such as retardation which were ignored in the earlier attempts discussed previously. Figure 3.1 illustrates a sphere, a disk and a triangle consisting of *N* elements ordered in a cubic lattice. Choosing larger number of elements to illustrate a nanoparticle, thus shortening the distance between elements, will result in more accurate results. However, for the case of large number of elements, calculations can be time consuming or impossible. Thus, there is always a tradeoff between the duration and accuracy of the calculations as in the case of many other computational methods used in any area of physics. It is clear from the figure that particles of any shape can be constructed and involved in the calculations by use of this approach.

The induced dipole P_i in each element in the presence of an applied plane wave field will be then,

$$\boldsymbol{P}_i = \alpha_i \boldsymbol{E}_{loc,i} \tag{3.8}$$

where α_i and $E_{loc,i}$ are the polarizabilities and local field around the elements, respectively. The local field around an element can be expressed as the superposition of the incident field and retarded fields due to other *N-1* elements in the entire domain. Since the elements forming the nanoparticles should be small compared to the wavelength of the incident light and the size of the nanoparticle,

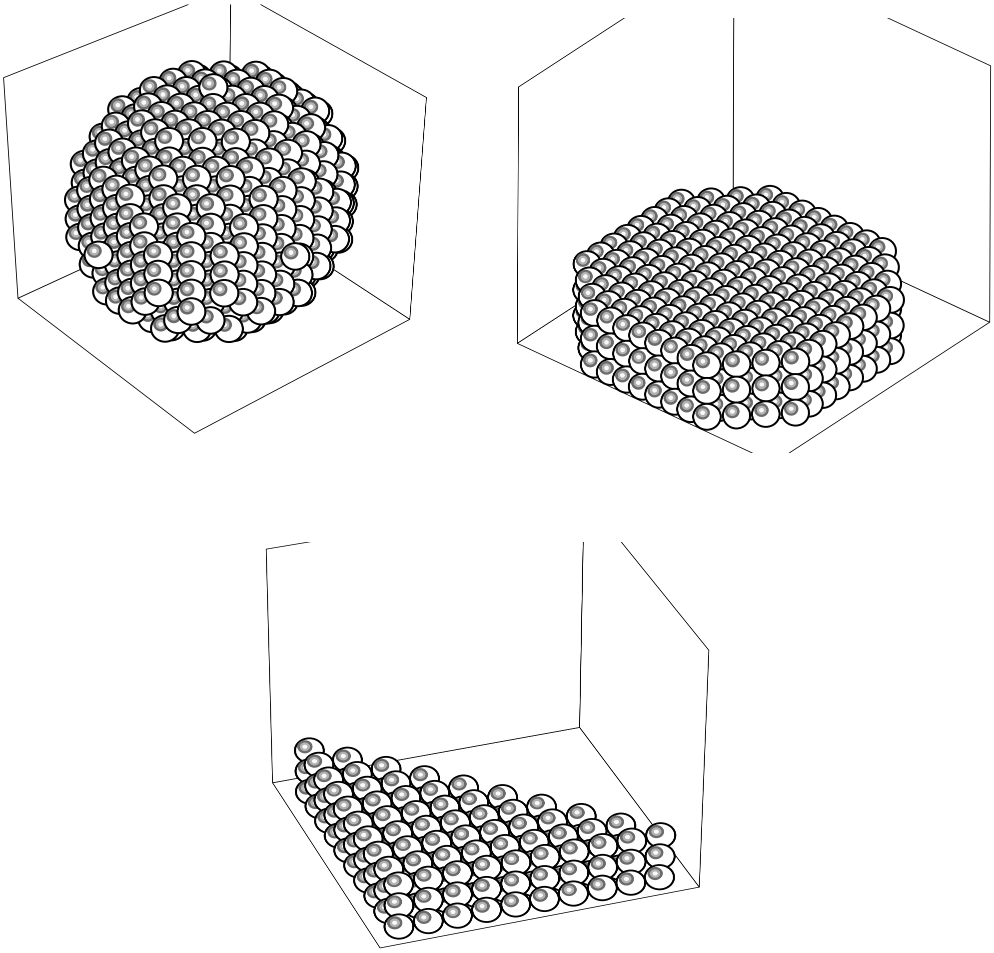

Figure 3.1: Representation of a sphere, disk and triangle with N polarizable elements. Nanoparticles considered in this study for DDA method are formed in this manner.

field from each contributor can be thought as an ideal dipole term. The local field given in equation (3.8) can be defined as,

$$\boldsymbol{E}_{loc,i} = \boldsymbol{E}_{inc,i} + \boldsymbol{E}_{dipole,i} \tag{3.9}$$

with an incident plane wave,

$$\boldsymbol{E}_{inc,i} = \boldsymbol{E}_0 exp(i\boldsymbol{k}.\boldsymbol{r}_i - i\omega t) \tag{3.10}$$

and contributions from all other elements,

$$\boldsymbol{E}_{dipole,i} = \sum_{i \neq j} \boldsymbol{A}_{ij} \,.\, \boldsymbol{P}_j \tag{3.11}$$

where the index, *i*, represents the element whose dipole moment is to be found and the index, *j*, denotes the other *N-1* elements. E_0 and k are the amplitude and wave vector of the incident field. Defining the distance between any two elements forming the particle as, $\boldsymbol{r}_{ij} \equiv \boldsymbol{r}_i - \boldsymbol{r}_j$, the interaction matrix given with the term A_{ij} can be found by,

$$\boldsymbol{A}_{ij} . \boldsymbol{P}_j = \frac{exp(ikr_{ij})}{{r_{ij}}^3} \times \left\{ k^2 r_{ij} \times \left(r_{ij} \times P_j \right) + \frac{(1 - ikr_{ij})}{{r_{ij}}^2} \left[{r_{ij}}^2 - 3 r_{ij} \left(r_{ij} . P_j \right) \right] \right\} \quad (i \neq j) \tag{3.12}$$

To illustrate the key relation of the method given in equation (3.9) in a simpler manner, it is possible to define,

$$A_{ii} = {\alpha_i}^{-1} \, . \tag{3.13}$$

The resulting formulation of the entire problem is then,

$$\sum_{j=1}^{N} A_{ij} \,.\, P_j = E_{inc,i} \quad (i = 1, \ldots, N) \tag{3.14}$$

By use of the equation (3.14), it is now possible to obtain a relation consisting of *N* homogeneous linear complex vector equations and find out the polarization vectors which will then provide us the necessary optical cross sections. The optical cross sections can be expressed in terms of $\boldsymbol{P}_i$,

$$C_{ext} = \frac{4\pi k}{|\boldsymbol{E}_{inc}|^2} \sum_{i=1}^{N} Im\left(\boldsymbol{E}^*{}_{inc,i} . \boldsymbol{P}_i \right) \tag{3.15a}$$

$$C_{abs} = \frac{4\pi k}{|\boldsymbol{E}_{inc}|^2} \sum_{i=1}^{N} \left\{ Im[P_i . ({\alpha_i}^{-1})^* {P_i}^*] - \frac{2}{3} k^3 P_i . {P_i}^* \right\} \tag{3.15b}$$

Of course the scattering cross section can be obtained by use of the same relation given in equation (3.7c). Although we will be concerned about the scattering of light by metal nanoparticles in this work, extinction cross sections of those particles will be modeled because of its simpler formulation. Fortunately, it is well known that for particles having relatively larger sizes, scattering cross section will be much more dominant in the extinction. Due to this fact, it will not be a costly simplification for our case to discuss the extinction cross sections of the particles with sizes larger than 80 nm of diameter.

Solving the problem of light interaction with a small particle with DDA method seems to be possible. However, as in the case of all approximations, one should be careful about the parameters involved in the calculations. To illustrate the material properties with a high accuracy, dipole polarizabilities assigned to infinitesimal elements forming the metal nanoparticle must be in agreement with the physical system. The lattice dispersion relation, proposed by Draine and Goodman, gives accurate results for the configurations considered in this work [41]. The idea behind the method is to find the dipole polarizability for an element that will provide the bulk dispersion relation of the material when ordered in an infinitely large cubic lattice. In the limit $kd \ll 1$, the polarizability of the particle can be approximated as,

$$\alpha^{LDR} \approx \frac{\alpha^{CM}}{1+\left(\alpha^{CM}/d^3\right)[(b_1+n^2 b_2+n^2 b_3 S)(kd)^2-(2/3)i(kd)^3]} \tag{3.16}$$

where α^{CM} is the Clausius-Mossotti polarizability and d is the lattice constant between elements. Constants involved in the expression are given as,

$$b_1 = -1.891531$$

$$b_2 = 0.1648469$$

$$b_3 = -1.7700004$$

$$S \equiv \sum_{i=1}^{3} \left(\widehat{k}_i \hat{e}_i\right)^2$$

where $\hat{k}$ and $\hat{e}$ are the unit vectors defining the propagation direction and polarization of the illuminating light.

Having obtained the necessary representations for optical quantities, we can now consider some examples to examine the effects of size, material and shape of the nanoparticles on the resonance conditions. Figure 3.2 gives the extinction efficiencies for silver spheres having diameters of 60 and 100 nm located in vacuum.

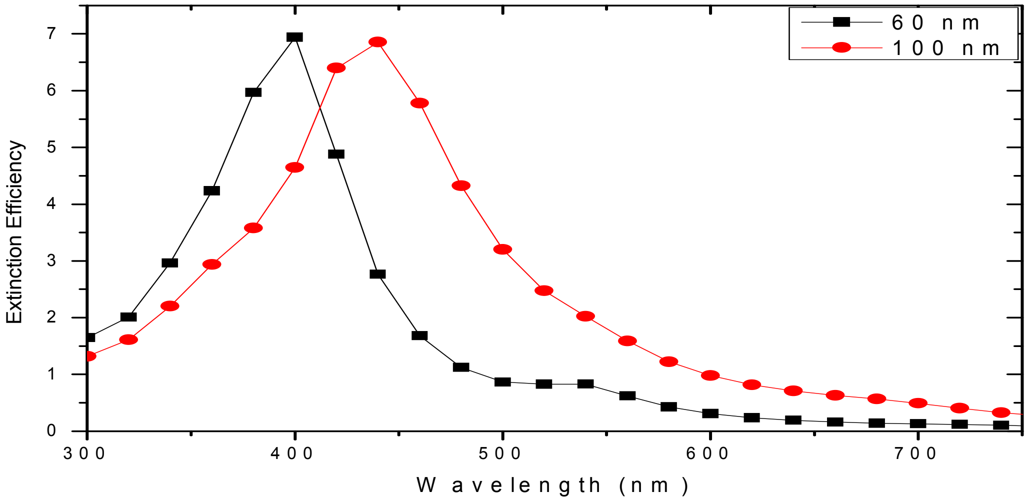

Figure 3.2: Extinction efficiencies for silver spheres having diameters of 60 and 100 nm located in vacuum.

It was mentioned in earlier discussions in this study that size effects can be observed significantly in the resonance peaks as a broadening due to the multipole emissions. In figure 3.2, where only the size of the nanoparticle was changed, DDA calculations show that both a red shift and broadening occur for larger nanoparticle. Simple cases are illustrated in figure 3.2 to ensure the agreement between the results obtained in this work with exact solutions given in studies referenced at the beginning of this chapter.

Calculation of extinction efficiency for gold nanoparticles having the same size and shape as in the previous example of silver particles provides us resonance conditions in the region around 530 nm in figure 3.3. The red shift and broadening of the peak with increasing size can be observed in the case of gold also. However; another red shift, being much more significant, can be seen easily.

Examining the real part of the dielectric constants of both metals, one can see the obvious reason for this shift which could also be noticed from the results of quasistatic approximation. Another difference between the data for silver and gold is the amplitude of the efficiencies. Relatively broader and weaker resonance peaks of gold nanoparticle can be attributed to the higher complex part of the dielectric constant.

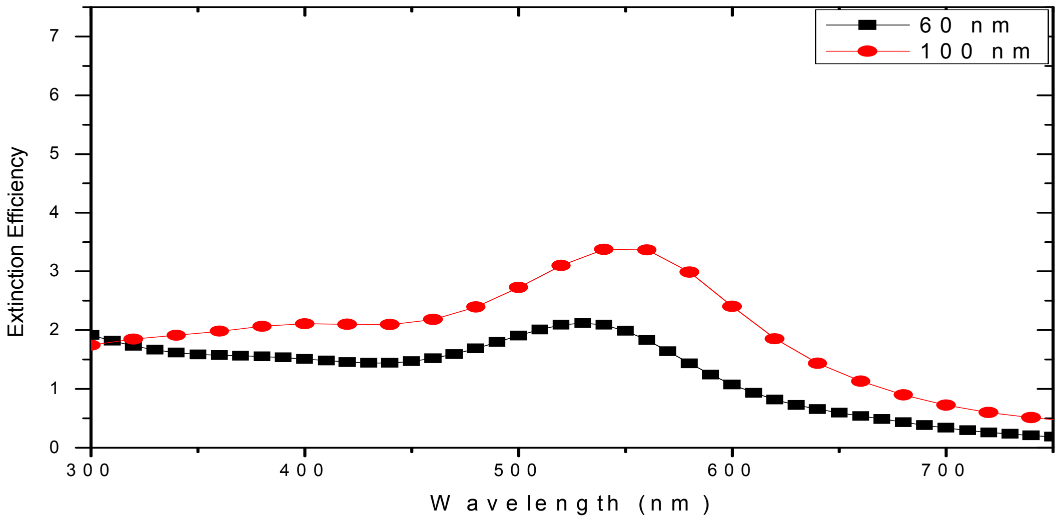

Figure 3.3: Extinction efficiencies for gold spheres having diameters of 60 and 100 nm located in vacuum.

In the expressions for the field outside the particle found from quasistatic approximation, the resonance condition emerged to be different for the cases of the sphere and the infinite cylinder. Although the shape of an infinite cylinder can be used to model a nanowire, we will be dealing with nano-disk shaped particles produced by electron beam lithography which cannot be approximated as an infinite cylinder. Figure 3.4 gives the extinction cross section for a silver nano-disk calculated with DDA method. The shape effect on the resonance condition can easily be noticed.

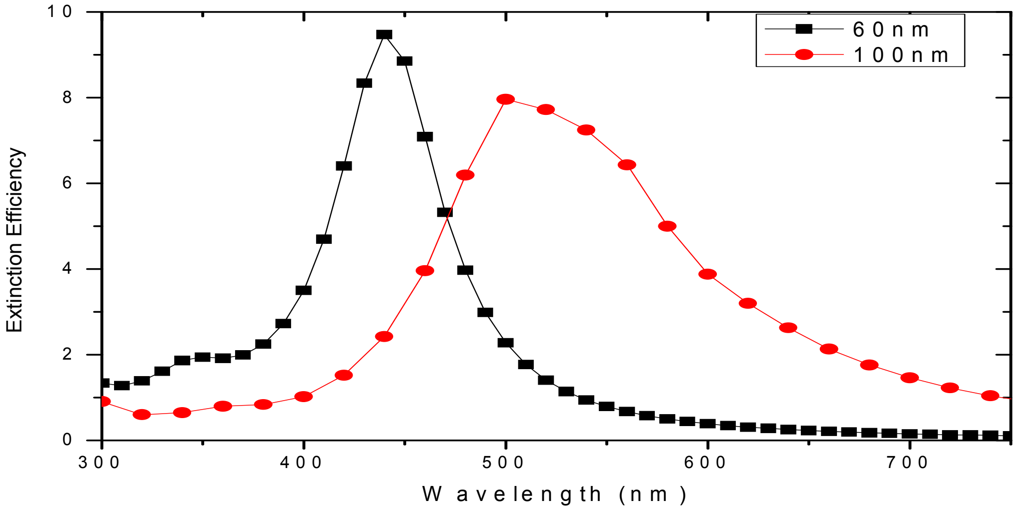

Figure 3.4: Silver disks having diameters of 60 and 100 nm of diameter located in vacuum. Resonance conditions are apparently different from the case of spheres.

The resonance peaks are observed to be red shifted when compared to the example of sphere silver nanoparticles. Another important result that can be predicted from the simulation results is that the extinction efficiencies for silver nanodisks are relatively high when compared to the sphere shaped silver nanoparticles. Extinction efficiencies are found to increase up to 10 times in the resonance wavelengths for nanodisk with diameter of 60 nm while it was found to be around 7 times in the case of spheres. However, as the radius of the particle increases, the efficiency decreases more rapidly in the disk case but it stays nearly constant at the peak position for the sphere.

Figure 3.5 illustrates the effect of the host medium the metal nanoparticles are residing in. Being obvious from the quasistatic approximation results also, increase in the dielectric constant of the medium is expected to red shift the resonance wavelength. Peak wavelength in the extinction efficiency of 100 nm silver disk in vacuum was found to be around 500 nm while it is found to be around 560 nm when the particle is located in water. In the case of quasistatic approximation, it was assumed that the host material was a nonabsorbing medium having only real part of dielectric constant. In practice, this assumption is not valid for some cases. In figure 3.5, presented with dashed lines, one can see the resonance condition for a 60 nm diameter silver nanodisk which is highly reduced and broadened due to the effect of conducting host medium.

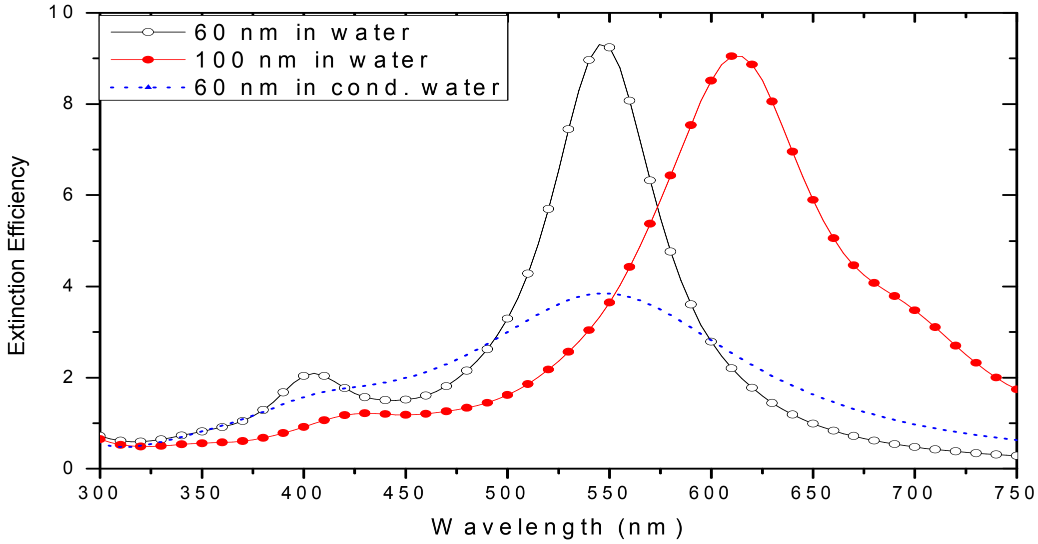

Figure 3.5: Silver nanodisks having diameter of 60 and 100 nm located in water, $\varepsilon = 1.77$, *(solid lines) and in illusive water having constant complex dielectric constant,* $\varepsilon = 1.77 + i0.5$.

Another check point for the validity of the code developed can be the case of an ellipsoid. Having lack of symmetry, an ellipsoid differs from the cylinders and spheres discussed up to now in this chapter. The asymmetrical axis of the particle is expected to result in two separate resonance peaks corresponding to wavelengths in resonance with each axis dimension. Figure 3.6 illustrates a simple case of an ellipsoid placed in vacuum.

It is clear that resonance conditions for both two axes are satisfied in the simulation. For a silver particle located in vacuum with dimensions of 60-120 nm, three different cases were considered. Firstly, an arbitrarily polarized light beam was considered to be incident on the nanoparticle. Given with the triangles in the figure, it can be seen that two peaks at around 400 and 650 nm are observed. To verify that those resonances are because of the two different dimensions included in the ellipse, two other cases for perpendicular polarizations were also examined. Circular disks with diameters 60 and 120 nm were simulated separately in a vacuum environment illuminated with polarized and arbitrarily polarized light. No difference due to the polarizations was examined for those circular samples while each resulted in resonances at wavelengths similar to those obtained in the ellipsoid case.

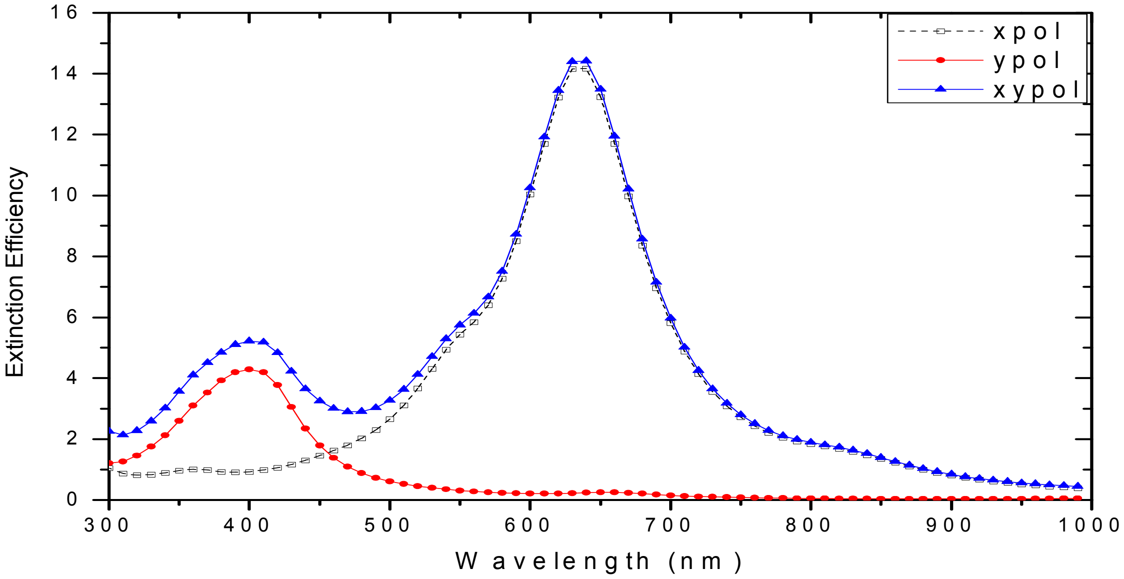

Figure 3.6: A silver ellipsoid nanoparticle with dimensions 60 and 120 nm located in vacuum. Extinction efficiency is computed for both polarizations of incident light and also for arbitrarily polarized case.

Finally, it should be reminded that manufacturing techniques employed in this study require the existence of a substrate layer that alters the symmetry of the boundary conditions. Since the dielectric constant around the particle will not be uniform, an effective constant should be determined to perform efficient simulations [42]. For simplicity; dielectric constants of all surrounding materials, ITO and air in most cases, were averaged with weight factors. The ratio of the contact areas between metal and each surrounding material to the whole area of the nanoparticle was used to determine the factors.

Considering illustrative examples with the software developed within this work based on the discrete dipole approximation, we obtained satisfactory results giving us the idea about the optical behavior of single metal nanoparticles having dimensions comparable to, but still smaller than, the wavelength of illumination. In order to obtain better accuracy, decreasing the volume occupied by each polarizable element, thus increasing the total number of elements included in the domain, will be needed as discussed above. However, large number of elements will increase the time required to obtain the results, and thus bring new challenges to increase the efficiency of the algorithms being used to solve linear homogeneous equations given in equation (3.14) [43,44].

CHAPTER 4

MANUFACTURING AND CHARACTERIZATION

Up to now, we have been dealing with the derivation of results for the interaction of light with metal nanoparticles from different points of view. To have a better understanding of the mechanisms taking part in the system and to verify the results found in the previous chapters, experimental studies are also included in this work. Electron Beam Lithography (EBL), being a slow but well controllable technique, is used to produce metal nanoparticle arrays having precise dimensions that will allow us to understand the effects of various parameters on the resonance behavior. Another well known nanofabrication technique, self assembly growth, will also be discussed at the beginning of this chapter. Finally, the optical setup developed to perform characterization experiments will be described at the end of the chapter.

4.1 Self Assembly Growth

Although the theory of interaction of light with small particles was almost completed in the mid of 1980's, experimental studies on this subject increased in last two decades due to the improvements in the field of nanomanufacturing. There are several techniques to produce metal nanoparticle assemblies to be used for plasmonic applications [45-47]. The most widely used techniques can be listed as Volmer-Weber growth which leads to growth of metal nanoparticles with a wide distribution of size and shape and Electron Beam Lithography (EBL) which is a relatively slow but precise means of obtaining monosized nanoparticles with well aligned distribution. In this study, both approaches have been applied and discussed.

Self assembly methods to produce nanoparticles are attractive due to its easiness and high speed compared to e-beam lithography. One can obtain a large area of metal nanodots in a relatively small amount of time, with an expense of high deviations in the size and shape of the particles [48].

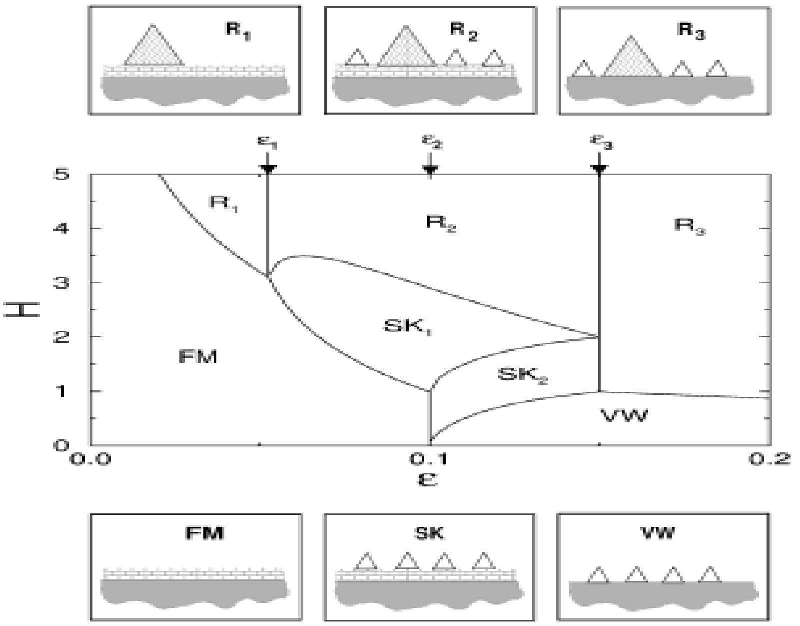

Figure 4.1: *Equilibrium phase diagram as a function of coverage, H, and misfit, ε. The panels on the top and bottom illustrate the morphology of the surface in the six growth modes. Empty triangles represent the stable islands where the shaded ones are for ripened islands* [49].

Growth of thin films on a substrate has three different mechanisms all depending on the lattice constants of the substrate and film materials. For the case of metallic nanoparticles, we will be interested in the Volmer Weber (VW) growth mechanism which results from a large lattice mismatch between the materials. As it can be observed from figure 4.1, VW growth occurs for a misfit of 10%. It can also be noticed from the same figure that the growth mechanism switches to Stranski-Krastanov (SK) mode where the growth of the film turns out to be in 2D or to ripened islands, presented with R, where nanodot dimensions cannot be controlled.

There are also studies aiming to solve the problem of size variations of the particles in self assembly techniques. Ouacha et. al. performed successful experiments to obtain gold nanoparticles having relatively small deviations in size by use of pulsed laser light [50]. One can expect high absorption of light at some wavelengths where the plasmonic effect becomes dominant. Using the optical characteristics of metal particles, samples were illuminated with 5.5 ns laser pulses having a wavelength of 751 nm. Since the size of the particles affects the absorption efficiency at specific wavelengths, it was expected that particles reaching a certain size would be highly absorbing the incident light. Those absorbing the incident light suffered from overheating and the resulting film was observed to be involving particles up to a certain size. The results obtained from the study can be considered as satisfactory since the method is still easy and consistent. Further investigation of the technique can be found in various other studies [51,52].

Figure 4.2 shows the SEM image of a sample of Au nanoparticles standing over quartz substrate produced with the self assembly method. Metal thin films coated over a substrate are observed to form nanoparticles with various shapes and dimensions when annealed.

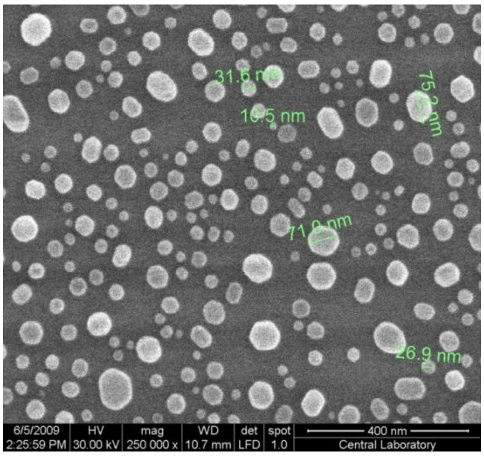

Figure 4.2: *SEM image of Au nanoparticles grown on quartz substrate with thermal evaporation followed by annealing.*

Films with varying thickness were fabricated using the thermal evaporation system illustrated in figure 4.3. Film thickness, annealing temperature and duration of the process are known to be affecting the sizes of nanoparticles obtained at the end of the day. Although the ability of production over a large area is an indispensible advantage for mass production, the size and shape variation that can be observed in figure 4.2 makes the method inconvenient for systematic studies of geometrical parameters.

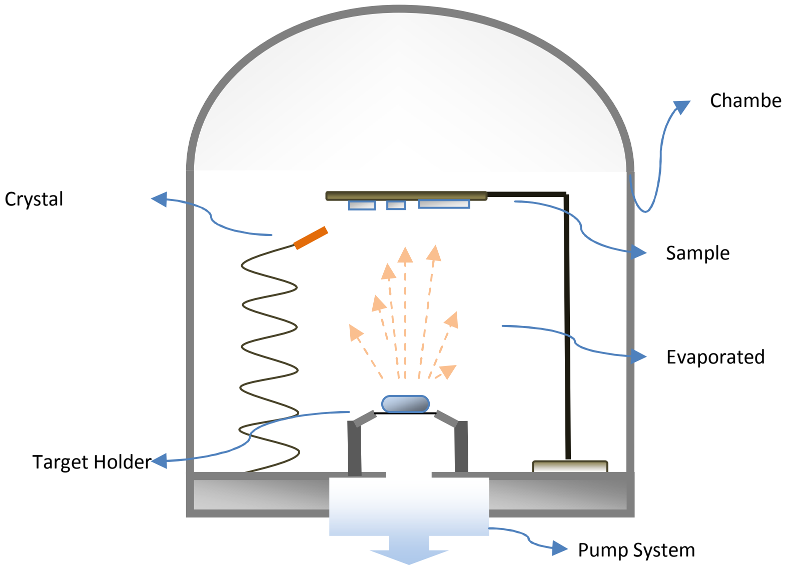

Figure 4.3: Resistive thermal evaporator system used in this work.

4.2 Electron Beam Lithography

As mentioned earlier in this study, electron beam lithography (EBL) provides well defined systems with controllable size and shape parameters. Since it is possible to obtain arrays of metal nanoparticles having desired geometrical properties [53-56], EBL was chosen to be the manufacturing method for samples used for optical transmittance and reflectance measurements. CamScan CS3200 scanning electron microscope was modified with a laser interferometric stage manufactured by Softsim and a pattern generator system from Xenos and used as an electron beam lithography system. Most of the nanoparticle arrays were patterned on microscope slides coated with thin Indium Tin Oxide (ITO) layers while patterns formed on bare slides and silicon wafers were also studied. Poly (methyl methacrylate) (PMMA) was used as an electron beam resist in the production period for all samples and coated with a spin coater at 6000 rpm on the substrate to obtain a layer thickness of approximately 100 nm. The thickness data provided by the manufacturer, MicroChem, for the product C2 950 PMMA versus spin speed is given in figure 4.4. Although the spin speed of 6000 rpm is out of the range in the graph, the desired thickness of 100 nm can be approximated. After spin coating, samples were baked in an oven at 170 °C for 30 minutes.

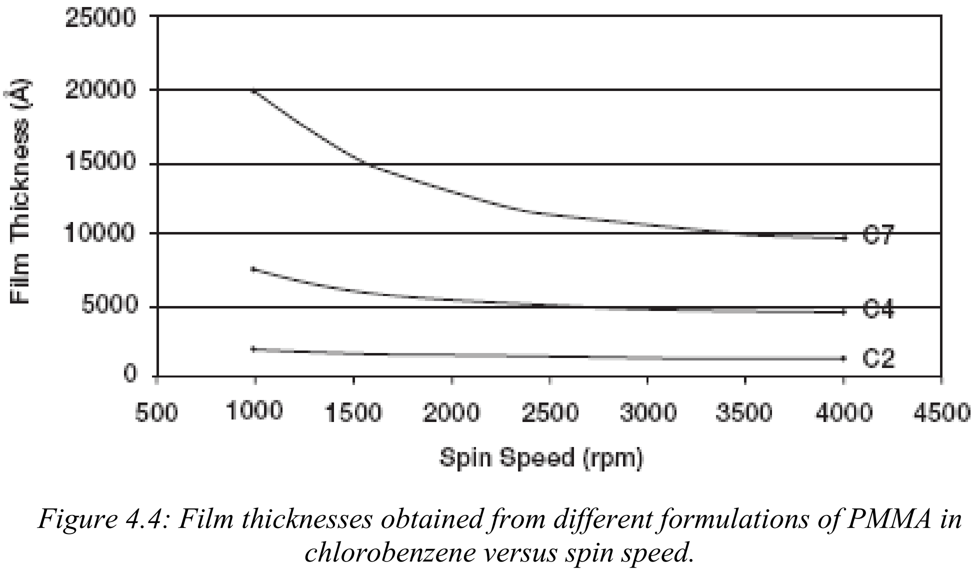

Figure 4.4: Film thicknesses obtained from different formulations of PMMA in chlorobenzene versus spin speed.

It is obvious from the film thickness data that any thickness of the PMMA layer could be obtained using different concentrations and different spin speeds. Thickness of 100 nm was chosen because of the small feature sizes needed where the diameter of the metal disks were required to be smaller than the wavelength of the incident light. At the very beginning of the study, circular patterns were given a try to form the disk shapes on the PMMA layer. However, the minimum sizes that could be obtained from those experiments could not shrink down to values smaller than 100 nm of diameter. Fortunately, smaller dimensions could be obtained by use of the proximity effect. At a given dose of electron exposure, one can obtain circles of different dimensions depending on the dwell time. Although the size and dwell time dependence at a fixed dose for a certain substrate is self consistent, this relation can be different for another substrate due to the electrical conductivities of those two materials. Figure 4.5 shows the scanning electron microscope (SEM) image of an array of nanoholes patterned on PMMA that will serve as a mask in further steps.

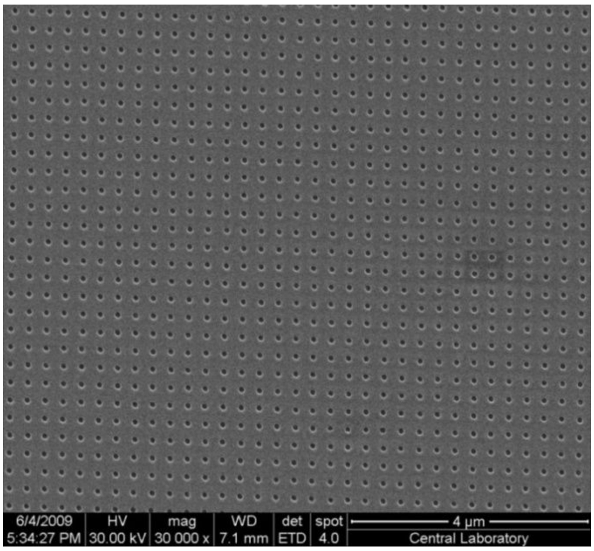

Figure 4.5: Array of nanoholes patterned on PMMA over an ITO coated microscope slide. 100 nm diameter holes with a period of 300 nm will serve as a mask in further steps.

One can see the obvious advantage of uniformity for the case of EBL technique that makes it a valuable method for discovering the effects of parameters on the optical behavior of small sized metal nanoparticles.

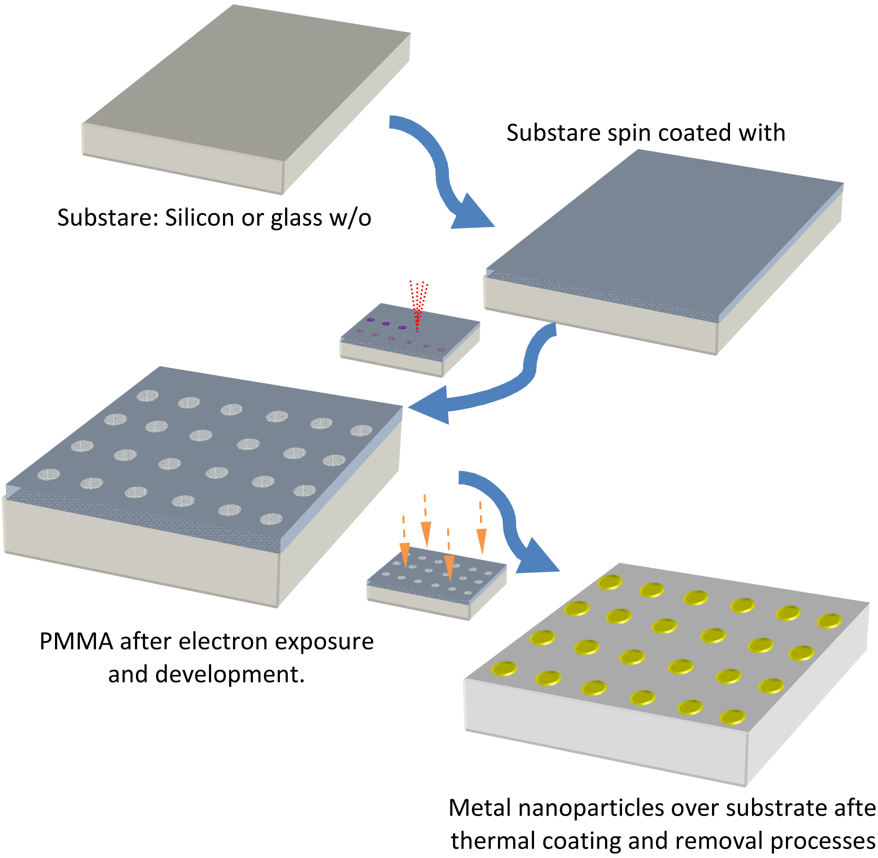

Figure 4.6: Illustration of EBL manufacturing steps to obtain array of metal nanoparticles.

After patterning the PMMA, sample was coated with a thin metal film of desired thickness by use of a resistive thermal evaporator system illustrated in figure 4.3 above. Gold and silver, having melting points around 1064 and 962 ^{o}C, could be coated with such a system with a growth rate of 0.8 angstrom/sec under a pressure of about 3-5x10^{-6} torr. The final step, after coating the patterned samples with thin metal film, is to remove the PMMA layer with metal film standing above by use of acetone. Although acetone seems to be a sufficiently strong chemical for

PMMA removal, it is sometimes required to keep the samples above room temperature for a smooth process. Especially for samples coated with gold much more efficient results were obtained from removal step performed in an oven heated to 100 ^{o}C. Figure 4.6 illustrates the steps of nanoparticle array manufacturing with EBL.

Procedure discussed above, also used for most of the cases in this work, can be named as the standard way of manufacturing by use of electron beam writing. However, for the case of bare microscope slides, it was not that straightforward to get regular patterns due to the insulating substrate. The charging effect for samples having poor conductivity is well known from SEM analysis of samples. Having poor conductivity, the samples are unfit for the flow of electrons that are used to change the chemical structure of the PMMA resulting in an accumulation of charge on the surface to be patterned. Due to coulomb interactions between the incident and accumulated electrons, the writing beam deflects from the destination point and significant deviations in the resulting pattern are observed at the end. To overcome charging effect and obtain conducting samples, a thin conducting layer is deposited over PMMA before the exposure. Electrons penetrating through the thin anti-static layer reach the resist and prepare the sample for removal step. Following e-beam writing, the thin conducting layer should be removed without damaging the PMMA to prevent any deformation in the pattern. It is also appropriate to make use of water vapor as the conducting layer for systems that are suitable. Another way of solving the problem of charging is to use a conducting polymer as the resist material and cancelling the additional steps required for the deposition and removal of thin conducting layers. Being one of the widely used and straightforward methods, a thin layer of gold was thermally coated over PMMA before the exposure for the case of bare microscope slides used in this work. In order to make the Au film transparent to the electron beam, its thickness was kept around 2 nm in the first stage of this study. Figure 4.7 gives the metal nanoparticles over bare glass obtained from samples having thin (2 nm) antistatic layer.

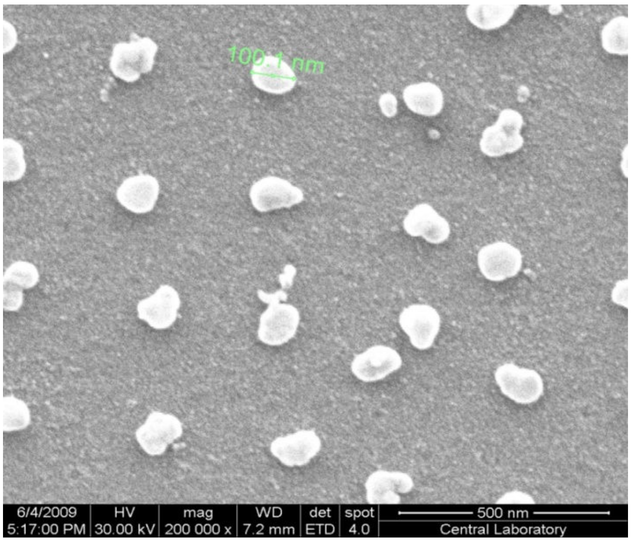

Figure 4.7: Metal nanoparticles over bare microscope slide patterned with an antistatic layer of 2 nm thick gold film. The resulting pattern is lack of symmetry because of the deviation in the path of electron beam due to charging of the sample.

However, as it can be seen from figure 4.7, 2 nm thick layer of thermally coated gold could not satisfy the desired conditions. This is indicating that very thin antistatic layer is not satisfactorily conducting. Due to the charging effect, that is altered to some extend but could not be removed completely, electrons in the incident beam are deflected from their original path and dots in the array are patterned to wrong coordinates forming a disordered structure. The solution to this problem is, obviously, to increase the thickness of the gold layer, thus increasing the conductivity. Of course, it is clear that layers having a large thickness will act as a strong barrier for the beam penetration and affect pattern generation negatively. Based on the results obtained from different trials, it can be concluded that gold films having thickness of around 4-5 nm act as good antistatic layers for pattern generation on insulating substrate.

Once having the substrate patterned, one should get rid of the gold layer above the PMMA to be able to develop the resist. Gold is known to be a noble metal having resistance to oxidation due to the electron configuration. Although it is relatively more difficult to remove gold layer when compared to other alternatives, it is not completely impossible. One of the several methods to remove the gold layer is to use a mixture of KI: I_2: H_2O. Both commercial and laboratory made gold etchants were used in this work providing high etch rates. For the case of a gold layer having thickness of 4 nm, 1-2 seconds of rinsing in the solution was found to be sufficient at room temperature for complete removal of the antistatic coating without damaging the exposed PMMA. Gold etchant prepared for the removal process has a mixing ratio of KI: I_2: H_2O = 4g: 1g: 40ml providing an etch rate of about 1 μm/min while the commercially available etchant, TFA, supplied from Transene has the etch rate of around 3 nm/sec at room temperatures.

Although the method of using a thin layer of conductor in the exposure process as an antistatic coating for the case of insulating substrates is straightforward, there are several tricks to avoid complications during the application due to the additional materials and steps included in the procedure. First of all, choosing a metal other than gold would probably bring instabilities for samples that are not immediately exposed and developed just after the deposition. However, choosing Au as the antistatic layer due to its stability also brought several difficulties. As mentioned above a solution of, KI: I_2: H_2O, is used to remove the thin Au layer introducing K and I_2 in to the system which should also be removed before further treatment of the sample. The simplest and most effective way is to rinse the sample in DI water long enough. Being sure that the sample is purified from any residual, one can proceed with the development step carried out with the conventional mixture of MIBK:IPA=1:2. However, it is found that development process fails for PMMA resists when the water rinsing procedure is followed. Figure 4.8a gives the image taken from an optical microscope just before the development of the sample.

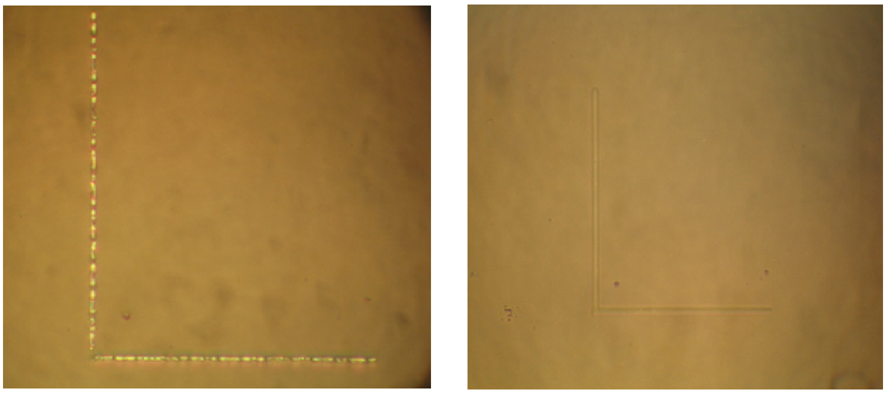

Figure 4.8: Images of samples before development w/o heat treatment taken with optical microscope.

One can easily notice the imperfections in the pattern before the development step. Although the sample is not developed yet, the pattern is observed to appear due to the long treatment of the sample. Any attempt to develop the sample at this stage yielded no result. Fortunately, it was observed that, a heat treatment process in an oven heated at 120 ^{o}C for a couple of minutes helps removing the residual as it can also be seen in figure 4.8b. Samples developed after a short annealing are observed to be well suited for further steps of metal deposition. It should be noted here that, the temperature should not exceed the value of 120^{o}C since the PMMA starts to melt and erases the pattern.

Upon considering the type of the solution to the problem, it can be concluded that due to the relatively long rinsing of the sample to remove residuals, water diffuses in to the region where chemical structure of the PMMA was changed because of the electron exposure or accumulates on the surface of patterned regions due to modified surface tension and this excess water, being a non-solvent of PMMA, prevents the development of the resist. Turbidity of the polymer in ternary systems consisting of water, acetone and PMMA is well known in the literature [57]. Considering the similarities between two materials, one can think of such a mechanism when acetone is replaced by MIBK in the system. When the substrate is heated, water content disappears as it can be seen from figure 4.8 and no more non-solvent exists during the development process. Figure 4.9 gives the SEM image of an array of Au nanoparticles standing over an insulating substrate, microscope slide, produced by use of the method explained above.

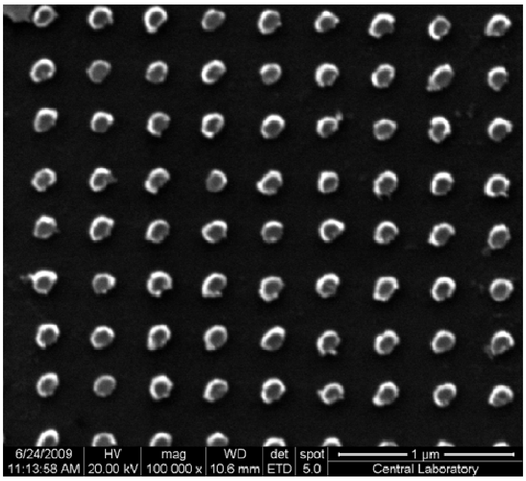

Figure 4.9: Au particle array over glass produced by use of a thermally deposited thin Au film as antistatic layer.

As mentioned above, disk shapes were patterned on the resist by use of ‘exaggerated dots’ to obtain higher resolution and form metal nanoparticles as small as required. Thus, main factors affecting the size of the resulting nanoparticles are the dwell time and dose of the exposure. As the dwell time increases, the amount of total charge arriving the resist increases. Thus, due to the proximity effect, charge disperses to a wider region. Alternatively, one can also increase the feature sizes by keeping a shorter dwell time but larger amount of dose. Of course, the resulting total amount of charge will again increase and the size of the features will be higher. However, for the latter case, it was observed that the minimum achievable feature sizes are relatively larger than former case with lower dose and larger dwell time. Also, the symmetry of individual particles is lost due to small dwell times. It can be said that, when the dwell time is larger the averaging over the ‘dot’ region balances the inhomogeneous charge destination that is mostly because of the astigmatism of the system. In the case of shorter dwell times, one cannot think about such an averaging thus the resulting nanoparticles are ellipses rather than circles from the bird’s eye view. On the other hand, high dose exposures bring the advantage of much shorter duration of the lithography process which is required when patterning large areas with less consumption of sources. Resulting particle diameters for various exposure parameters are given in tables 4.10 – 4.12 for microscope slides coated with 20nm ITO layer.

Table 4.10: Feature sizes obtained by use of different exposure parameters on glass coated with 20 nm ITO layer.

20 nm ITO coated Glass,790pA		Diameter (nm)		
Dwell Time (μs)	Dose (fC)	Period: 200	Period: 300	Period: 400
27.5	21.7	120-140	85-100	75
30	23.7	160-170	100-120	70-100
32.5	25.7	-----	105-125	80-110
35	27.7	-----	110-130	115-125
37.5	29.7	-----	115-140	105-140
40	31.7	-----	120-145	115-130
42.5	33.7	-----	135-165	120-140
45	35.7	-----	145-165	130-140

The use of thin ITO layers on the surface of glass substrates provides a conducting surface and prevents charging as mentioned before. Also, being transparent in the optical region of the electromagnetic spectrum, ITO is ideal for optical characterization. Exposure parameters and corresponding feature sizes given in table 4.10 indicate that it is possible to obtain larger disks by simply increasing the dwell time. However, due to the high current and short dwell times, resulting features are lack of axial symmetry. Another very important effect of the exposure parameters can be noticed from the same data. The resulting dimensions are also dependent on the period, sometimes called as the lattice constant, of the nanoparticle array.

Due to the proximity effect, exposed area of the resist is affected by the neighboring regions for the case of smaller periods and the feature sizes in the developed resist are found to be larger when compared to the arrays having larger periods when all other parameters are kept constant. This simply explains the failure of having nanoparticle arrays for doses higher than 23.7 fC for the case of 200 nm period. When the size of the features reached the value of the lattice constant, holes in the resist after the development disappeared leaving an empty frame of the nanoparticle array. As a result, after the removal of the PMMA, no particles are left behind on the surface of the sample. In the case of larger lattice constants where features are well separated, exposed areas are less affected by the neighboring regions resulting in smaller sizes. For instance, dwell time of 32.5 μs with a current of 790 pA resulted in an empty frame which helps us expect particle sizes of approximately 190 nm for the array having period of 200 nm.

On the other hand, keeping all parameters constant, arrays having periods of 300 and 400 nm were consisting of particles having approximate diameters of 115 and 90 nm, respectively. The same conclusion can be done for any other dose parameters in the mentioned table. Using the same substrate, exposures with lower currents are also performed. Table 4.11 gives the parameters and corresponding feature sizes of a lithography run for a current of 150 pA on the ITO coated glass. Data given for an array having lattice constant of 200 nm indicates that the value of the current makes significant changes in the resulting pattern. Feature sizes obtained from nearly the same doses are found to be much smaller when compared to the exposures with current values of about 790 pA. Although the maximum dose value used in the case of 150 pA is higher than the maximum value given in the former case, none of the particles reached sizes that would affect the resulting pattern.

Table 4.11: Resulting feature sizes for the case of a current of 150 pA on ITO coated glass.

20 nm ITO coated Glass, 150 pA		Diameter (nm)
Dwell Time (µs)	Dose (fC)	Period: 200
105	16	90
135	20	100
160	23	110
185	27	120
215	32	130
240	35	140
260	39	160

Another advantage of lower currents is the averaging effect due to higher dwell times as mentioned before in this chapter. Data given for a beam current of 150 pA verifies the averaging effect, i.e., the total charge dispersed over exposed area alters the asymmetrical axes of the resulting cylinders. Figure 4.12 gives the SEM images of metal nanoparticles patterned on ITO coated glass substrates with beam currents of 790 and 80 pA. Axial symmetry of particles produced with lower beam current and larger dwell time can be noticed very clearly.

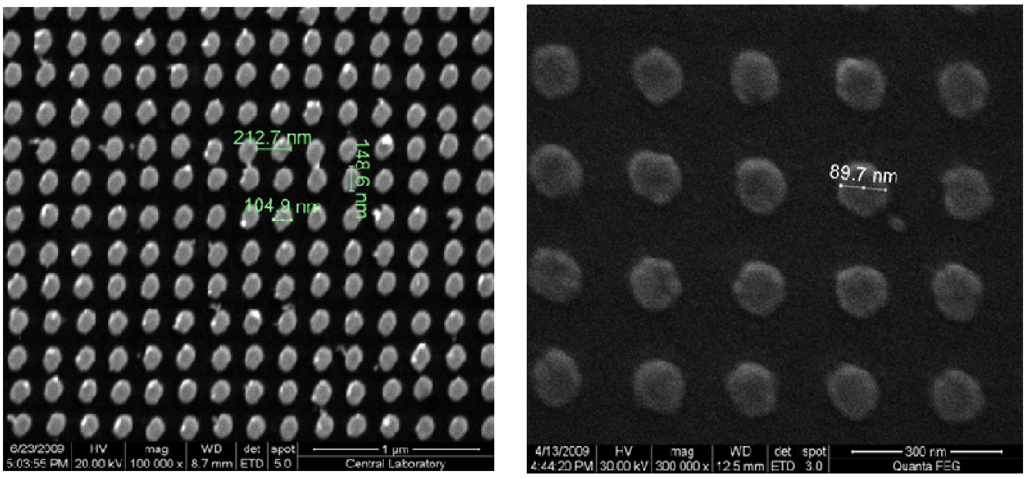

Figure 4.12: SEM images of metal nanoparticles patterned over ITO coated glass with different beam currents.

However, it should be remembered that total duration of exposures for such low beam currents exceeds tens of hours for arrays having large dimensions which are sometimes needed where focusing light to the sample area is not a practical issue. For those cases, due to the long operation periods, instabilities in the beam current are observed because of overheating of the tungsten filament and other components in the system. Those variations in the beam current are obviously responsible for the size variations of the nanoparticles within the same array, extinguishing the main advantage of the electron beam lithography technique. Table 4.13 gives the data for another relatively low current exposure on the same sample. Having almost the same relation between the dose of exposure and the resulting particle sizes with the 150 pA beam current case, 90 pA current data indicates that the effect of current to the dose – size relation is not simply linear. Considering both three data given in tables 4.10 – 4.13, one can conclude that, current values higher than some threshold alters the dose-size relations most probably due to charging effect. When the rate of charge removal from the exposed surface is lower than the charge injection, accumulated charges create a coulombic field dispersing the incident electron beam to a relatively larger area, which results in larger feature size. Fortunately, since the sample is not a poor conductor but only deficient of removing the incident charge as fast as required, the charging effect introduced in figure 4.7 is not observed in currently discussed results.

Table 4.13: Resulting feature size for the case of a beam current of 90 pA on ITO coated glass.

20 nm ITO coated Glass, 90 pA		Diameter (nm)
Dwell Time (μs)	Dose (fC)	Period: 200
100	9	-----
150	14	65
200	18	90
250	23	110
300	28	125

It can also be seen that minimum feature size obtained with a beam current of 90 pA for 20 kV is 65 nm for 200 nm period. Considering the whole data presented up to now, one can predict that reducing the beam current could provide the ability to obtain smaller particle dimensions. Although it seems to be feasible, more experiments should be performed with higher and lower current values to determine the minimum achievable dimensions experimentally. Of course, the minimum achievable size is limited by many characteristic parameters of the system. Sizes down to 25 nm can be considered as the minimum limit for typical EBL systems.

Being different in nature than the already mentioned sample, bare glasses coated with a thin layer of Au as antistatic coating should also be addressed here. Table 4.14 gives the data for such a sample under exposure with a beam current of 90 pA as in the case of the previous example. The main difference for the bare glass case is that, incident electron beam first faces the thin Au layer that acts as a barrier. Electrons penetrating the thin Au layer then enter the resist region and help forming the pattern. However, scattering of electrons should also be considered in this case. Although the antistatic layer is so thin that it lets most of the electrons pass through, one cannot simply assume that beam shape is not affected. Furthermore, electrons penetrating the PMMA no more face a conducting substrate as in the case of ITO coated glass or silicon samples. So, some more time should be given to electrons to diffuse back to the conducting Au layer which is grounded. Both two facts can be considered to be responsible for the larger dimensions obtained in the bare glass with antistatic layer case.

Relatively larger sizes when compared to the previous case is obvious in the data given for bare glass substrate verifying the discussion made about the effects of thin layer coated over the PMMA coated glass. A solution to prevent these effects could be to deposit the Au layer before the PMMA to obtain a structure very similar to the ITO coated substrates. However, both high electrical conductance and low optical transparency of gold films make it impossible to observe plasmonic effects. Referring figure 3.5, where the resonance condition for a silver nanodisk placed in an 'illusively' conducting medium is presented, one can predict that the resonance peak would be highly degraded. Conducting polymers designed as resists for EBL eliminate those antistatic layers and their effects. However, before using such materials for lithography purposes, their resolution should be compared to that of PMMA.

Table 4.14: Resulting feature size for the case of a beam current of 90 pA on bare glass coated with thin antistatic Au layer.

4 nm Au coated Glass, 90 pA		Diameter (nm)		
Dwell Time (μs)	Dose (fC)	Period: 200	Period: 300	Period: 400
100	9	110	105	-----
150	14	160	145	120
200	18	-----	150	135

Exposure parameters affecting the feature sizes obtained at the end are discussed and information required to produce nanoparticles with dimensions suitable to characterize localized surface plasmon resonances in optical regions of the electromagnetic spectrum is obtained. Minimum particle size obtained during the studies is a diameter of approximately 40 nm over ITO coated glass substrate. Figure 4.15 gives the SEM image of this sample.

Particles having diameters smaller than 40 nm could be obtained by simply increasing the voltage applied from 20 kV to 50 kV. However, referring to figure 2.5, one can conclude that metal nanoparticles with smaller dimensions would absorb the incident light rather than scattering back to the host medium, which is not the preferred when scattering is more desirable for a specific application such as solar cells. Thus, particles having dimensions larger than 60 nm are mainly studied in this work.

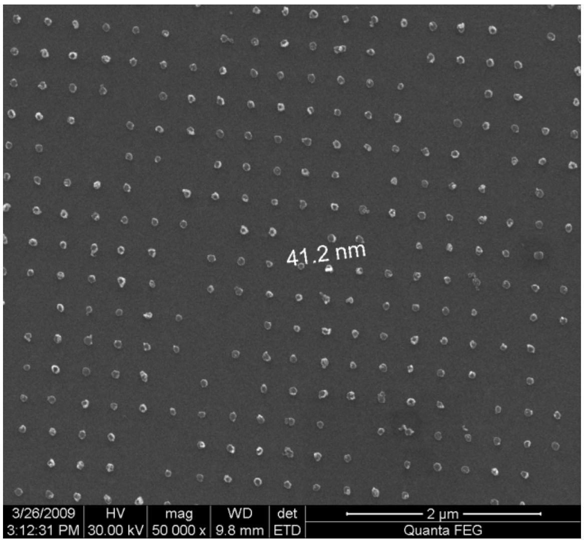

Figure 4.15: SEM image of silver nanoparticles having approximately 40 nm diameter patterned over ITO coated glass substrate.

Optical behavior of metal nanoparticles manufactured by electron beam lithography will be discussed in the following chapters where the results of transmittance and reflectance experiments are presented. Before proceeding to the results of optical characterization, we will be introducing the setup constructed to perform experiments.

4.3 Optical Characterization

Once having the nanoparticle arrays over substrates, next step is to examine the optical behavior of the samples. Optical characterization of nanosized metal particle arrays/clusters is of critical importance and several techniques, including numerical tools, are developed to obtain efficient results [58-63]. At the very beginning of the work, a setup consisting of a fiber coupled light source and a monochromator with a CCD camera was used for optical characterization. Light beam passing through the fiber was focused with a collimator attached to the end of the guide to the nanoparticle array. Then, transmitted light through the sample was spectrally resolved by the monochromator and transmitted to the CCD camera. However, this kind of an optical setup requires large sample area which causes serious difficulties during the manufacturing steps. Since the magnification of the fiber collimator was not high enough, arrays having area of 600x600 μm^2 were needed to obtain stable transmittance data. Obviously; patterning such a large area with EBL, especially for feature sizes of about 100 nm, with small deviations in size is not convenient due to the excessive exposure time. Another disadvantage of such an optical setup is the inadequacy of the configuration to the reflectance measurements. For the sake of simplicity, an optical microscope with both reflection and transmission mode was coupled to a monochromator through a multimode fiber as illustrated in figure 4.16.

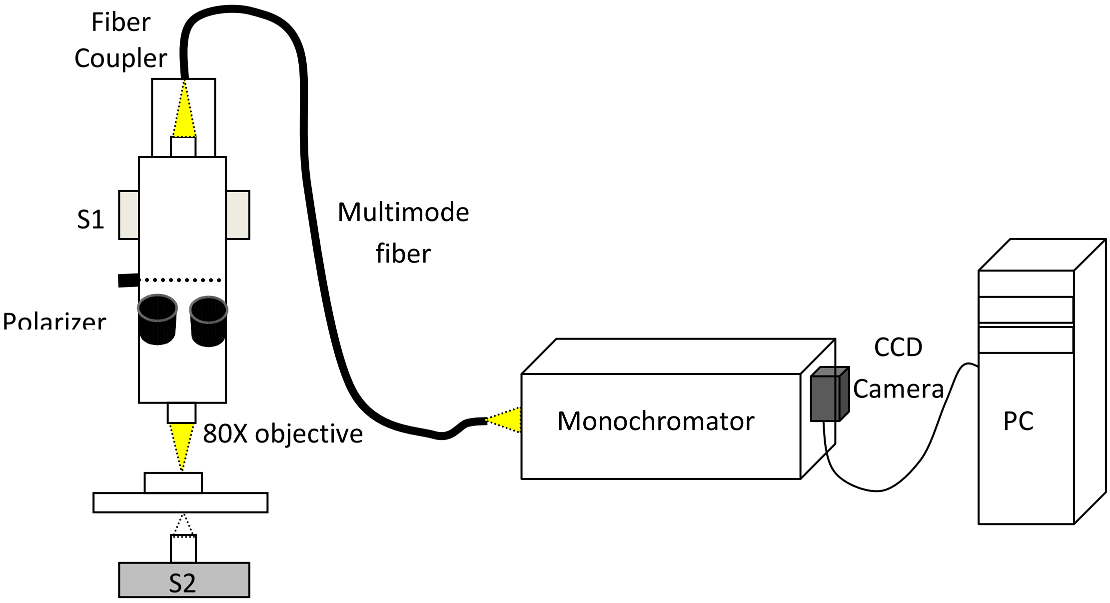

Figure 4.16: Illustration of the optical setup used for characterization.

By the use of the setup illustrated in figure 4.16, where S1 and S2 denote sources 1 and 2 respectively, it turned out to be possible to perform both reflectance and transmittance measurements for arrays having much smaller areas when compared to the previous case described above. Also including a polarizer, the microscope made it possible to investigate the polarization dependence of reflection spectra for nanoparticle arrays having dimensions down to 100x100 μm^2. Replacing the fiber coupler with a digital camera, both reflectance and transmittance pictures could be obtained. Figure 4.17 shows the images of nanoparticle arrays prepared for both two setups discussed above in this section, taken with a digital camera inserted into the microscope system in the reflection mode. The optical reflectance data and transmission picture of those samples will be given in the following chapter.

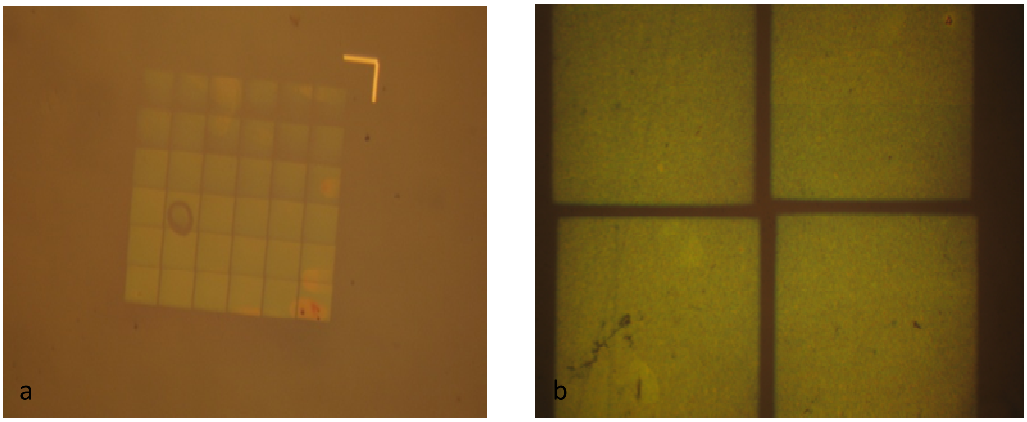

Figure 4.17: Reflection images of nanoparticle arrays with dimensions of (a) 600x600 and (b) 200x200 μm^2 *produced for two different optical setups described above.*

Having relatively small sizes, both silver nanoparticle arrays have resonances around 530 nm which results in a dipole emission of green light both inside and outside the substrate. Using the reflection mode of the microscope, one can observe the scattered light from those nanoparticles. The important point at this stage is the uniformity obtained in the case of the sample which is prepared for the microscope based setup. Due to the relatively small area, exposure time of the pattern is nine times shorter that prevents the deviation in the dose of the electron beam due to the heating of the filament source or charging of the other elements used for electron optics. Regions between neighboring fields are left blank to ensure that borders are not exposed multiple times due to intersection that prevents the clear removal of the metal film coated after patterning.

CHAPTER 5

OPTICAL BEHAVIOR OF METAL NANOPARTICLES

After a brief discussion of light interaction with metal nanoparticles with dimensions smaller than the wavelength, we can now proceed with the results obtained from the optical experiments. To begin with; the transmittance data obtained from samples produced with two methods, self assembly and electron beam lithography, should be compared to notice the difference between the bandwidths. Figure 5.1 gives the transmittance data of two Au arrays.

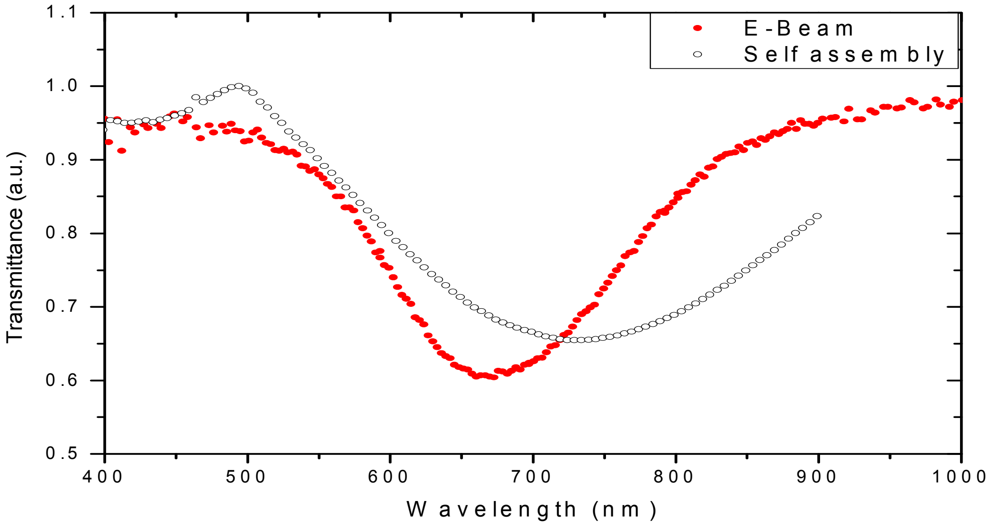

Figure 5.1: Transmittance data of two samples produced with self assembly and electron beam lithography methods.

The size deviation in the sample produced with self assembly method does not allow us to work with a well defined nanoparticle size, while in the case of electron beam lithography; one can precisely generate any pattern with narrow size distribution. The sample prepared by self assembly cover almost the entire visible and near infrared region. Since we have Au nanoparticles, the reduction in the transmitted signal begins around 520 nm which corresponds to the plasma frequency of Au. It is well known that resonance behavior cannot be observed for wavelengths shorter than plasma wavelength due to the fact that the dielectric function has positive values in this region. Referring to figure 4.2; one can conclude that the particles with sizes from 2 nm to 100 nm, or to larger dimensions for samples produced with different parameters, are responsible for the large bandwidth obtained from the self assembled sample. On the other hand, pattern produced with EBL provides a narrower bandwidth since the deviation of the particle sizes is much smaller. One should also take into account that the particles patterned with EBL have ellipsoidal shape, bringing a larger bandwidth when compared to circular disks. Unfortunately, polarizer in the setup cannot be used in the transmittance experiments preventing us to distinguish the peaks belonging to two different axes. Discussions on this issue will be given in the proceeding sections.

Another discussion to be made before considering the nanoparticle arrays is the effect of the ITO layer coated on the microscope slides to prevent charging effect due to insulating glass substrate. Insulating substrates are usually coated with a thin conducting oxide (ITO) in the EBL process to avoid charging effects. With high transmittance in the visible and near infrared region, ITO is a quite well material to be adapted in studies which include optical experiments. However, in our case, one should also take the optical constants of the material into account since resonance conditions are strongly affected by the constants of the surrounding medium. ITO is known to have a varying refractive index, from 1.8 to 2, in the visible region and have a very small extinction coefficient. Relatively higher refractive index of the ITO layer when compared to glass which has an index of around 1.517 can be thought to affect the position of the resonance peak. Also, having a small but nonzero extinction coefficient, it can be predicted that a slight degradation and broadening will occur in the resonance peak. Figure 5.2 gives the simulated data for both cases where Au nanoparticles standing over glass microscope slides w/o ITO layer are considered. As expected, resonance peak in the case of ITO coated sample is slightly red shifted. However, a slight enhancement is observed when compared to the case of bare glass. Considering equations 2.12b and 2.13b, one can see that an increase in the refractive index of the host material is expected to result in an increase in the magnitude of the field outside the sphere which directly affects the extinction efficiency. So, it can be concluded that the enhancement due to the higher refractive index of the host material is more dominant than the degradation due to the nonzero extinction coefficient.

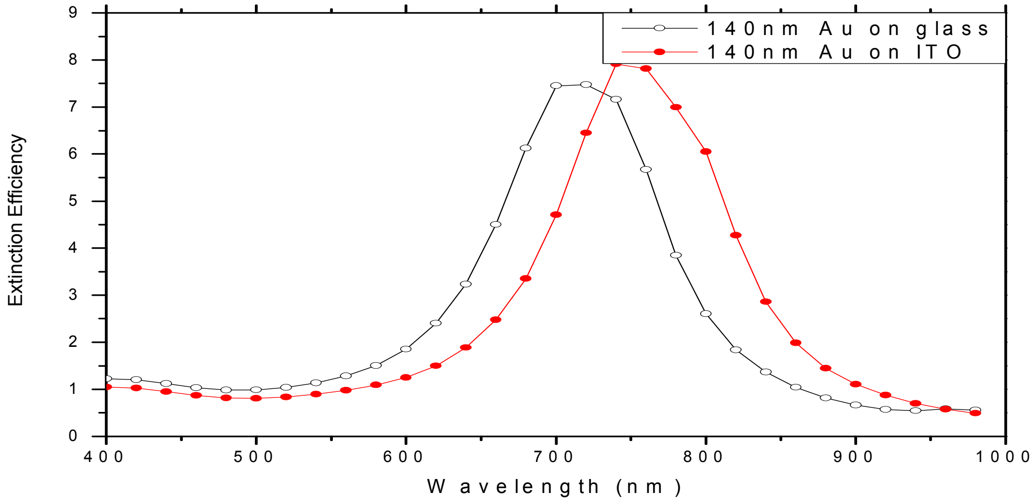

Figure 5.2: DDA simulation of Au nanoparticle over glass w/o ITO layer.

To check the effect of the thin conducting layer, reflectance of identical Au nanoparticle arrays over bare and ITO coated microscope slides are examined. Sample with bare glass is prepared by use of a 4 nm thick Au antistatic layer as explained in the previous chapter. Figure 5.3 gives the reflectance data for arrays of Au nanoparticles with 140 nm diameter patterned over glass substrates w/o ITO layer. Examining the peaks for both cases, one can notice that red shift of the peak position predicted by the simulation cannot be observed. The main reason for the inconsistency is the broadening of the resonance peak due to the coupling of neighboring nanoparticles which are separated from each other with a lattice constant of 200 nm. In the case of simulation, where only one single nanoparticle is considered due to domain size limitations, the resulting peaks are found to be narrower allowing us to observe the shift in the peak. Furthermore, the simulated nanoparticles are perfect circular disks while particles in the sample are ellipsoids with a slight difference in the axes which, again, results in a broadening of the peak.

On the other hand, expected enhancement of the peak is found to be much higher than the simulation results. The peak value for reflectance in the ITO case is three times the peak value for bare glass. Obviously, such a strong enhancement in the reflectance cannot be attributed to the dielectric constant change in the surrounding medium. Most probably, the additional boundary layer between the ITO film and glass is the main reason for the enhanced reflectance peak. In the regions outside the resonance, incident light can be considered to be normal to the boundary layer. However, incident light with wavelength in the resonance region will strongly interact with the metal nanoparticles and a dipole, or multipole depending on the size of the target, emission will be observed. Thus, scattered light will gain an angle of incidence which will obviously result in a higher reflection from the boundary between ITO layer and glass. As a result, the total effect of a thin conducting layer on the substrate is observed to be an enhanced reflectance from the samples. Possible shifts or broadening of the peak due to the dielectric constant of ITO are within the deviations expected from coupling of particles and geometrical imperfections.

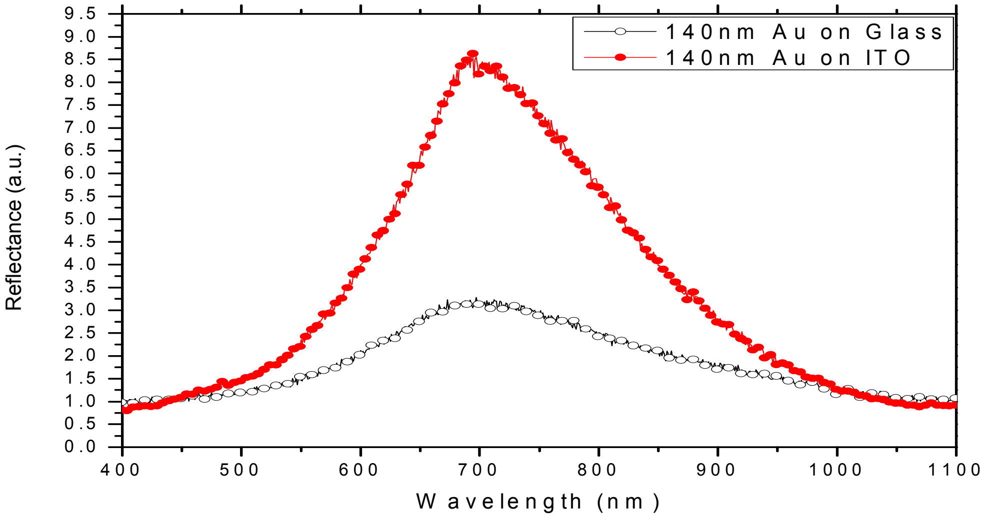

Figure 5.3: Reflectance data of Au nanoparticles patterned over glass substrates w/o ITO layer.

We can now proceed with characterization of more specific samples. As it is already mentioned, the most widely used metals for plasmonic applications are Au and Ag due to their superior optical characteristics. For this reason, we have focused on nanoparticle arrays consisting of Au and Ag in this study. In each section focused on specific materials, common parameters affecting the resonance behavior will also be considered.

5.1 Gold Nanoparticle Arrays

Scattering cross section of Au was found to be weaker than Ag by use of quasistatic approximation in chapter 2 and presented in figure 2.7. However, the 'lifetime' of Au nanoparticles is known to be much longer than Ag since gold is oxidized less due to the electronic structure. Stability issue obviously forces people to consider Au rather than Ag for practical applications of LSPR. In this section, we will discuss the reflectance measurements of arrays consisting of Au nanoparticles. First of all, the size of the nanoparticle is known to affect the resonance conditions strongly. Figure 5.4 gives the reflectance data obtained from an array of Au nanoparticles with 20 nm thickness. Sizes of the nanoparticles vary between 60 to 145 nm and lattice constant of the array is 200 nm.

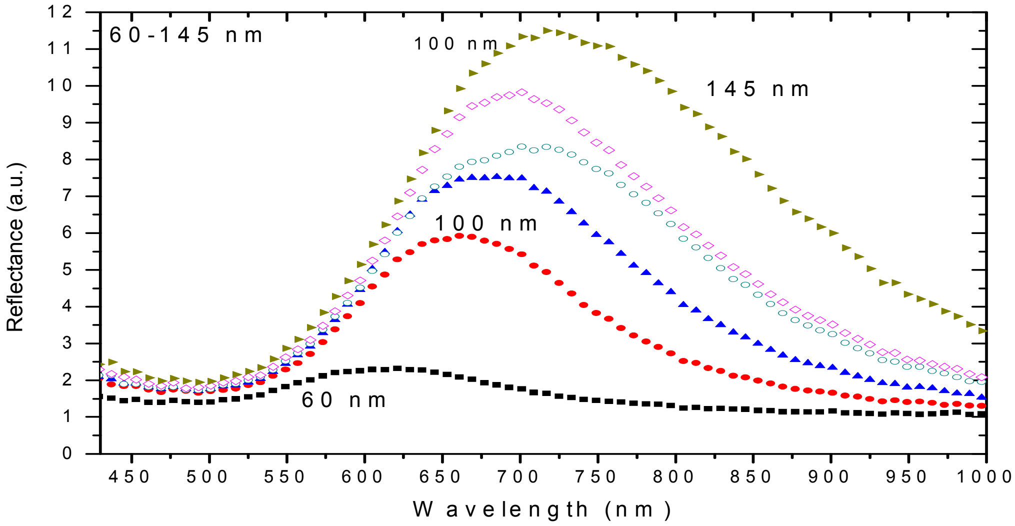

Figure 5.4: Au nanoparticle array with a lattice constant of 200 nm patterned over ITO coated glass. Nanoparticle thicknesses are 20 nm and diameters vary between 60-145 nm.

It can be noticed that the bandwidth of the peaks are larger than expected. The reason of such a broadening is the fact that particles are not simply circular nanodisks but ellipsoids with different lengths of axes. Saving this issue to the next discussion, we will focus on the size effects on the peaks. As expected from the simple theory, increasing size will result in a larger areal density of metal which will, in turn, result in a larger peak value. Also, an increase in the size of the nanoparticle will lead to higher order modes due to retardation effects because of the fact that the particle is no more ‘much smaller’ than the wavelength of incident light. Those higher modes will obviously broaden the resonance peak. Furthermore, since the lattice constant is kept constant, particles in the array will get closer to each other as their sizes become larger and coupling effect will be more dominant leading to broadening [64].

Turning back to the discussion on the effect of ellipsoidal shape to the resonance peak, one can check for polarization dependent transmittance data of the same sample. Figure 5.5 gives the Au nanoparticle array with lattice constant of 200 nm and particle diameters of 80 and 110 nm.

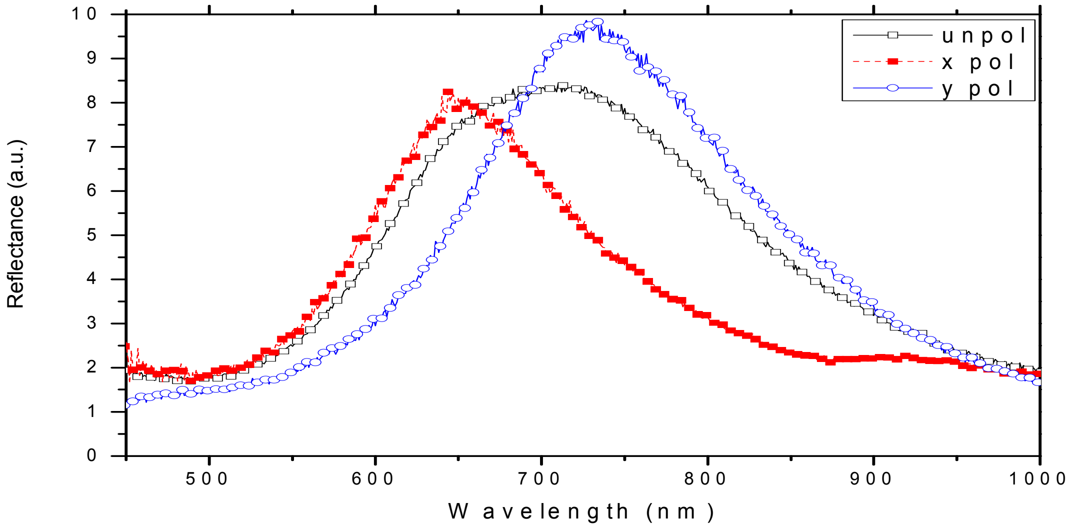

Figure 5.5: Ellipsoidal Au nanoparticles with axes 80 and 110 nm, with lattice constant of 200 nm over ITO coated glass.

We see that peaks corresponding to different axis can be distinguished clearly. Peak corresponding to shorter axis is observed to be around 630 nm while resonance due to larger axis peaks around 730 nm. However, since the aspect ratio of the particles is not that large, peaks corresponding to different axes are close to each other. In addition, 200 nm of lattice constant is so small that coupling between particles prevents the observation of separate peaks. In order to see whether the observed polarization behavior can be modeled theoretically, we have performed DDA simulations for disturbed geometries. Figure 5.6 presents the data obtained for an Au particle with axes 80 and 110 nm, located on ITO coated glass.

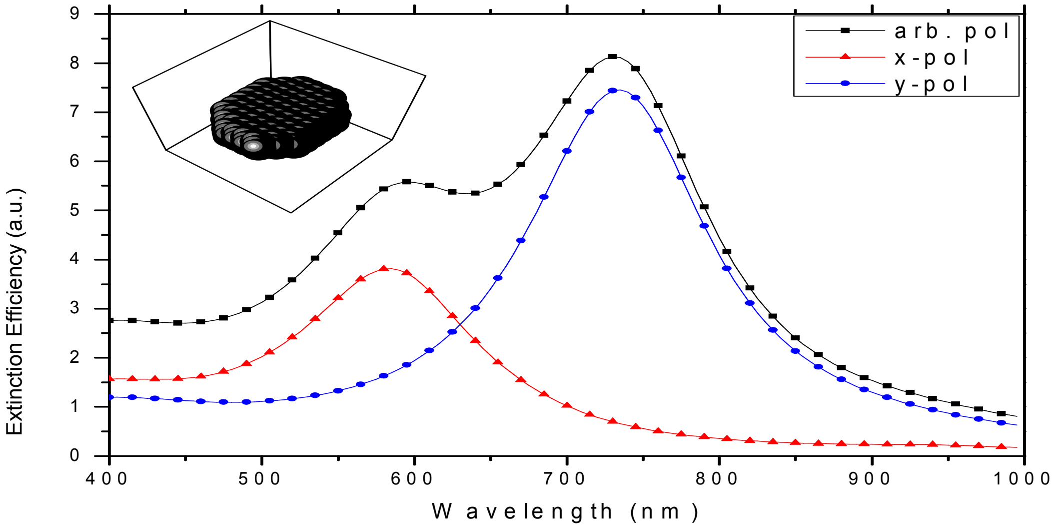

Figure 5.6: DDA simulation of Au ellipsoid with axes of 80-110 nm and height of 20 nm located on ITO coated glass.

DDA simulation for a single Au nanoparticle provides sufficient data to predict the behavior of an array consisting of those particles. Peaks due to both axes can be distinguished from simulations including both polarized and arbitrarily polarized incident light. However, resonance peak due to the shorter axis is blue shifted when compared to the experimental results. Two different facts should be considered as the reason for such a deviation. First of all, particle sizes in the array are measured from SEM pictures from individual nanoparticles randomly chosen from a large array of them, which can be somehow different from the other elements in the array. In addition, representing smaller feature sizes with relatively larger dipole elements, thus using less polarizable elements than required, will result in a deformation of the shape of the particle. So, having the same sizes of dipole elements in both axes due to the cubic lattice requirement, it can be thought that larger axis could be represented well enough to get correct peak position while resonance due to shorter axis had some deviations. Another fact to be discussed at this stage is that the peaks in the arbitrarily polarized case of the DDA simulation can be distinguished while a single broad peak is observed in the experiment. The reason is obviously the coupling of particles in the array that affects the results of reflectance measurement but cannot be observed in the simulations where only one nanoparticle is considered. To support this idea, reflectance data for an array with a lattice constant of 300 nm consisting of Au nanoparticles is given in figure 5.7.

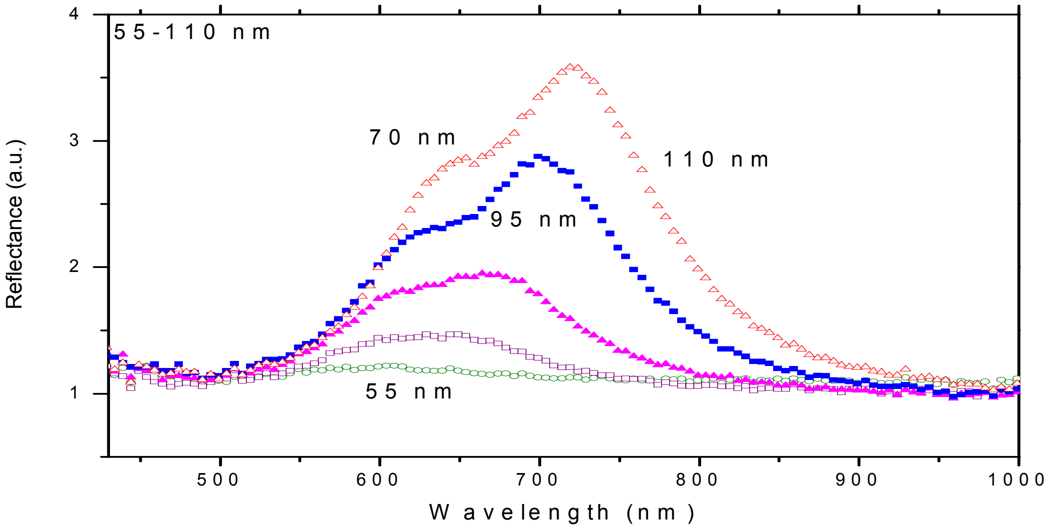

Figure 5.7: Au nanoparticle arrays with lattice constant of 300 nm. Particles are ellipsoids having dimensions varying between 55-110 nm.

Due to the larger lattice constant, nanoparticles in the array are coupled less with each other when compared to the particles in the previous example. One can obviously distinguish the peaks due to different axes of the spheroids in the case of a 300 nm separation between neighboring particles. Thus, one can conclude that as the distance between particles is increased, coupling effect reduces and the characteristic of the resonance peak approaches the single particle case.

Array consisting of largest nanoparticles having axes dimensions 80–110 nm, represented with open triangles in figure 5.7, shows resonance at wavelengths of around 630 and 730 nm. Those wavelengths are very similar to the values obtained in the case of the sample with 200 nm lattice constant given in figure 5.5. It is now worth considering the effect of array period on the resonance conditions. Considering arrays consisting of ellipsoidal nanoparticles having dimensions 80-

110 nm and varying periods between 200 and 400 nm, we can proceed with the discussion on Au nanoparticle arrays. Figure 5.8 presents the polarization dependent reflectance of those Au nanoparticle arrays.

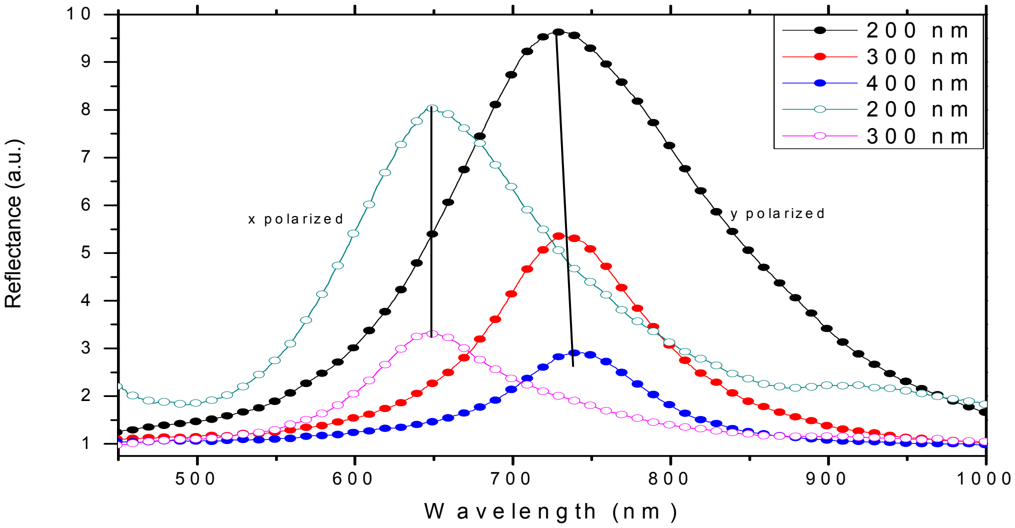

Figure 5.8: Reflectance from arrays with same nanoparticle sizes, 80-110 nm, but varying lattice constants form 200 to 400 nm.

First of all, it is obvious that the peak values for arrays with larger lattice constants are reduced due to the lower metal coverage on the surface. On the other hand, a slight red shift is observed as the period increases for both polarizations. In addition, peaks tend to narrow for the case of larger separations which can be attributed to the reduced coupling between particles as discussed above. This mechanism is shown to result in very narrow resonances numerically when well designed patterns are considered [65]. Resonance peaks for the case of unpolarized incident light are not plotted in the figure for the sake of clarity. However, it should be mentioned that the same shift in the peak position and narrowing in the bandwidth can be observed in this case also.

To observe the resonance behavior of nanoparticles more efficiently, it is better considering arrays with relatively larger periods. Broadening of the peaks due to coupling makes it more difficult to observe differences related to the size of the particle. Also, existence of two separate peaks due to different axis dimensions affects the results negatively in the same manner. Figure 5.9, providing the resonance data of Au array with lattice constant of 300 nm for the case of polarized incident light, give the chance to examine the effect of increasing nanoparticle size on the resonance conditions.

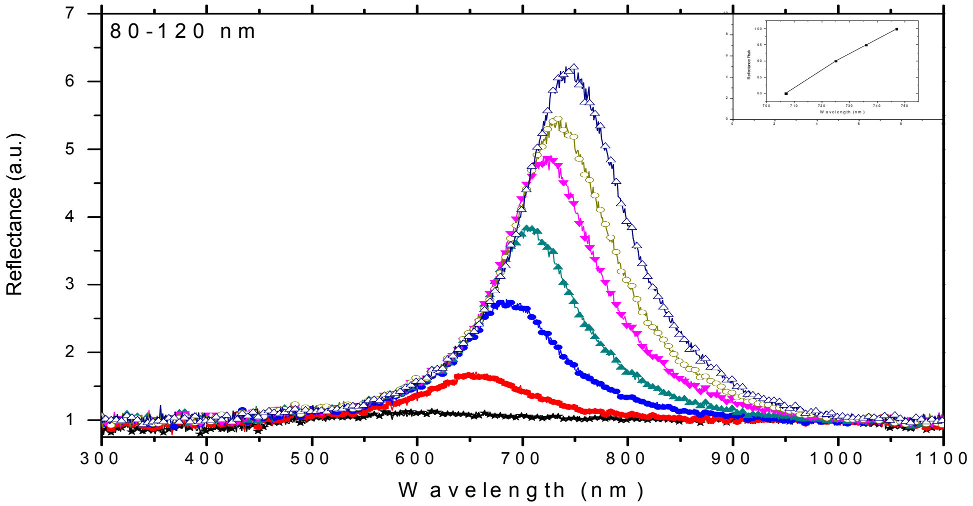

Figure 5.9: Reflectance spectra of ellipsoidal nanoparticles illuminated with polarized light with axes varying between 80-120 nm. Inset shows the dependence of peak wavelength to the particle size.

Red shift in the peak position with increasing size can be noticed easily. Also broadening of the peaks due to larger sizes is clearly observable in figure 5.9. Peaks are observed to have Lorentzian shape with slightly increasing location and scaling parameters. Figure 5.10 gives the DDA results for Au circular nanodisks having diameters between 80 and 120 nm.

Although the peak shapes are very similar to the experimental results and red shift is also observed, the peak positions do not match exactly with the experimental values. The main reason for the deviation in the resonance condition is the dielectric constants used both for the metal itself and the surrounding medium. As discussed earlier in this chapter, optical constants of ITO vary throughout the visible region. Since the deviation in the constants is not too large, refractive index of ITO is taken to be 1.9 for simplicity. Also, being dependent on the growth conditions, exact dielectric constants of Au could not be employed in the simulations. Values for the dielectric constants of Au in the simulations are calculated with the use of the models discussed in chapter 2 of this study. In addition; simulations, being performed for one single particle, cannot take the coupling effect into account which broadens the peak as discussed earlier in this chapter. Considering all those facts, results obtained from the DDA simulations can be found sufficiently consistent with the experimental findings.

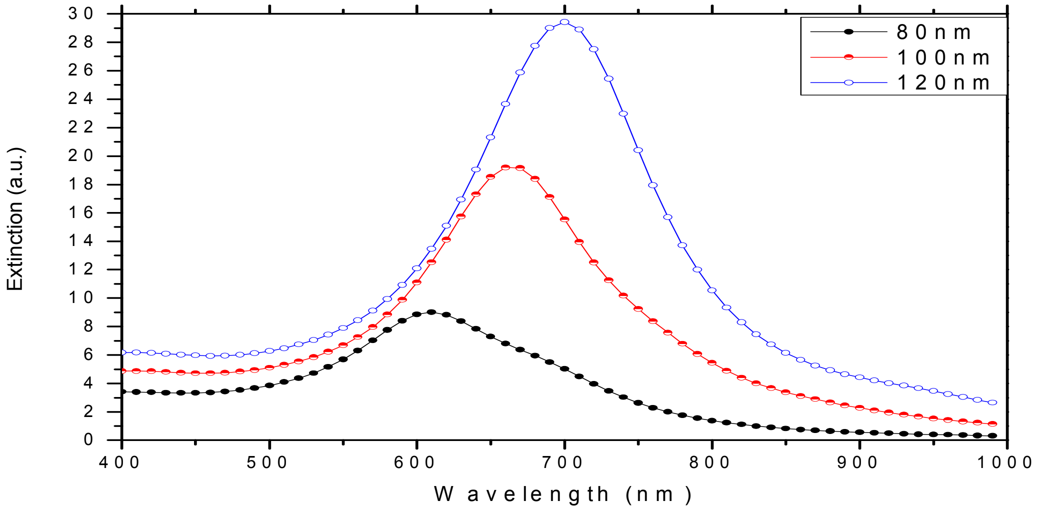

Figure 5.10: Extinction of Au nanodisks with increasing diameters located on ITO coated glass computed with DDA simulations.

Another parameter affecting the resonance conditions of the nanoparticle arrays is the thickness of the nanoparticles forming the arrays. Keeping the diameter of the nanodisk constant and increasing the height is found to affect the resonance behavior. First of all, it should be considered that the array will include a higher amount of metal that will result in a larger peak value when compared to particles with same diameters but smaller thicknesses. Figure 5.11 provides the reflectance spectra of Au nanoparticles with the same diameter but different thicknesses.

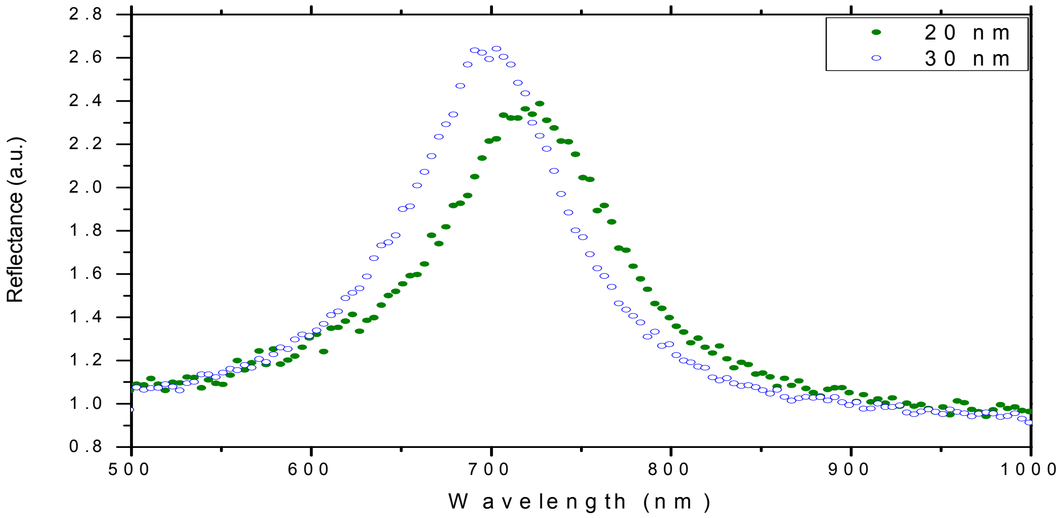

Figure 5.11: Reflectance of Au nanoparticle arrays with all parameters kept constants except the thicknesses.

Consisting of ellipsoidal nanodisks under polarized light with corresponding axis lengths of 90 nm, both arrays have lattice constants of 400 nm. Blue shift in the peak position of the thicker nanoparticles is clearly observed in the reflectance measurements performed with the optical setup. Also, increase in the peak value due to higher metal content is clear. Figure 5.12 presents the same condition simulated for Au nanoparticles with different thicknesses.

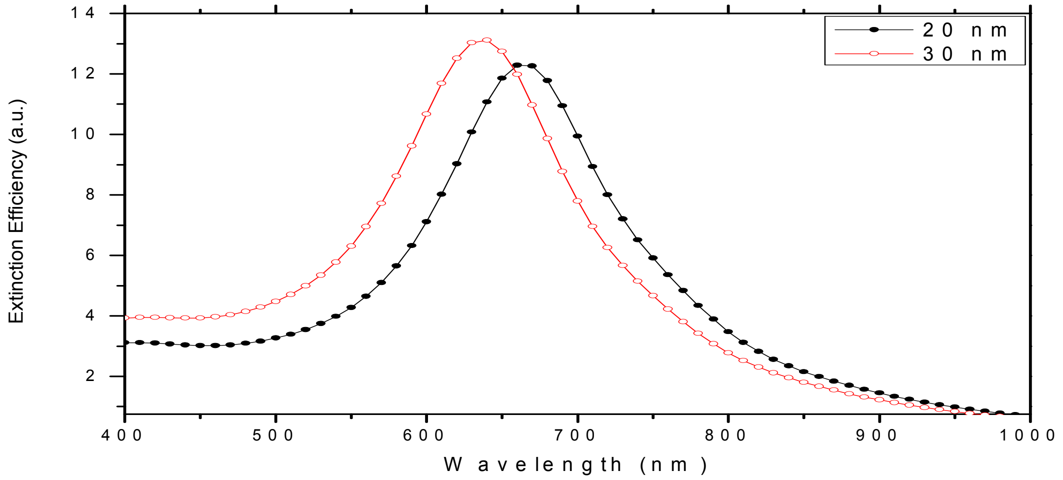

Figure 5.12: Effect of thickness on the resonance peak for single Au nanoparticles.

Results of the DDA simulations, performed for different thicknesses of Au nanoparticle having all other parameters constant, agrees well with the experimental data. Almost the same blue shift and slight increase in the peak for thicker disks is observed in the simulations.

We can now proceed with the discussions for Au nanoparticle arrays having thicknesses of 30 nm. Of course, one should expect the peak shapes to be the same with the previous examples of thinner particles except the slight blue shift and enhancement of the peak values. Figure 5.13 gives the data for 30 nm thick ellipsoidal Au nanoparticles with sizes between 90 and 200 nm.

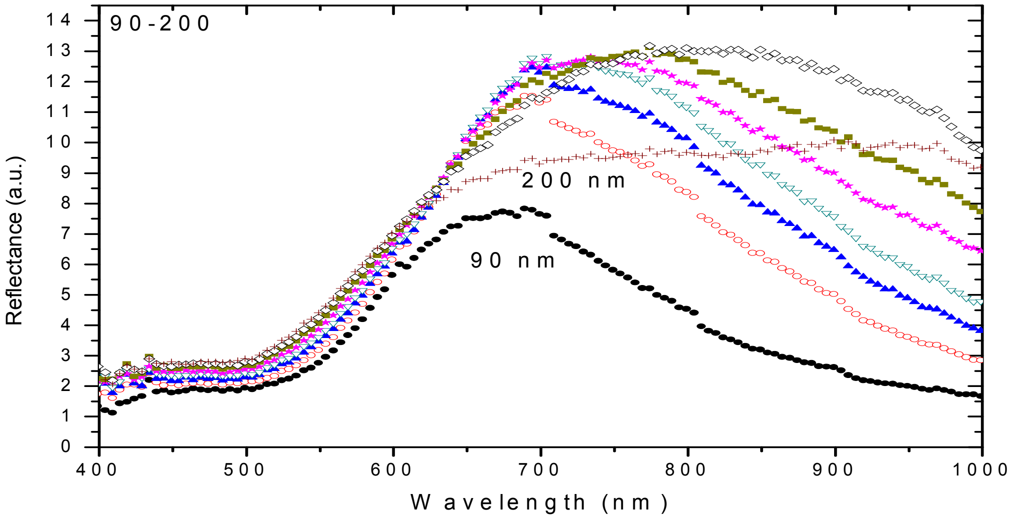

Figure 5.13: 30 nm thick ellipsoidal Au nanoparticles with varying diameters.

Reflectance data given in figure 5.13 belongs to an array with a lattice constant of 200 nm. However, the size of larger nanoparticles become close to the period of the array and peaks are so broadened that one cannot observe the resonance behavior due to the overlap between neighboring particles. For the case of largest nanoparticles; the reflectance data, represented with cross (+) in figure 5.13, no more shows resonance condition. Instead, the nanoparticle array acts as a mirror which highly reflects the incident light in the region below plasma frequency. Also, the amount of reflection is almost constant in this region. As a result, no more localized surface plasmons are observed due to the contacts between the disks. Figure 5.14 gives the SEM picture of the array with nanodisks having dimensions close to the period.

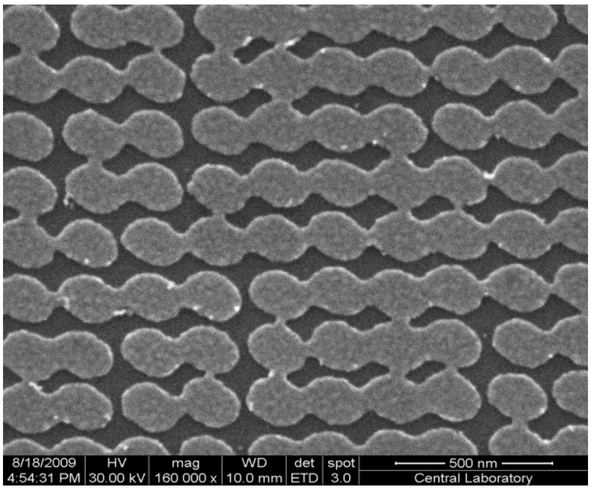

Figure 5.14: Au ellipsoids with diameters close to the lattice parameter.

In figure 5.5, polarization components in the reflectance data of an array of ellipsoidal Au nanoparticles is given and discussed for 20 nm thick samples. However, the slight decrease in the peak intensity in the case of unpolarized light was not mentioned during the discussions. Now, for the case of 30 nm thick Au nanoparticles, higher values of reflectance peaks are achieved due to higher metal content and a clear resonance behavior is observed even for patterns with lattice constant of 400 nm. Figure 5.15 shows the reflectance spectra for 30 nm thick ellipsoidal Au nanoparticles illuminated with unpolarized and polarized light.

Considering the polarization components and unpolarized reflectance, one can easily notice the decrease in the intensity for the latter case. It can be deduced from figure 5.15 that the resonance maximum is negatively affected by the perpendicularly polarized incident light. In other words, oscillations of electrons in orthogonal directions through the nanoparticles are not completely independent. Although further examination is required to conclude this discussion, it is worth a try in an independent study since high speed optical modulations can be achieved by use of this behavior.

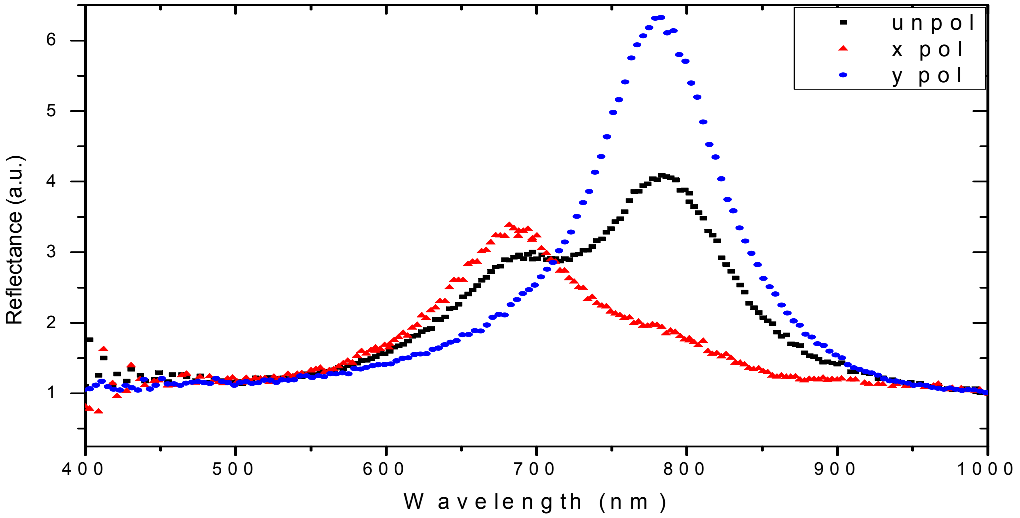

Figure 5.15: Reflectance spectra of ellipsoidal Au nanoparticles with lattice constant of 400 nm.

Before proceeding to next section which will be on the results obtained from Ag nanoparticle arrays, we should make a comparison between Au and Ag nanoparticles keeping all other parameters constant. Based on the quasistatic approximation, such a comparison is already done in figure 2.7 for Au and Ag spheres located in vacuum. The result was in agreement with the predictions and scattering from the Ag sphere was found to be higher. Figure 5.16 provides the extinction spectra for Au and Ag nanodisks located on ITO coated microscope slide.

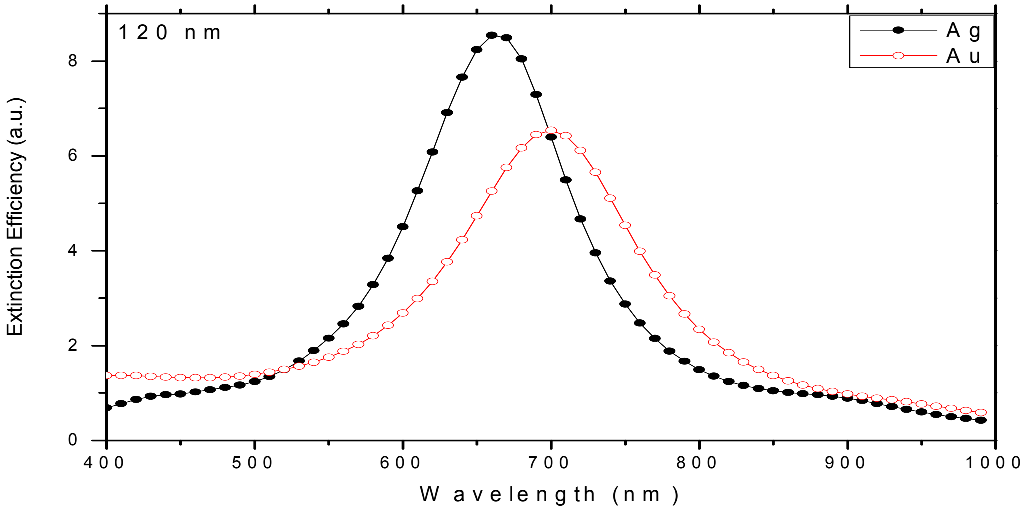

Figure 5.16: Extinction efficiency of 120 nm Au and Ag nanodisks located on ITO coated glass, simulated with DDA.

DDA simulations for 120 nm nanodisks also verify the higher efficiencies that can be obtained by use of Ag. It was mentioned in chapter two that relatively higher imaginary part of complex dielectric function of Au is responsible for the reduced peak intensity. Also, due to the difference between the dielectric functions of two metals, Ag has a resonance at relatively smaller wavelengths. Although both the theory and simulations verify the superior optical properties of Ag nanoparticles, one should also consider the technical aspects of them for real applications.

5.2 Silver Nanoparticle Arrays

After the long discussion on the optical properties of Au nanoparticle arrays in the previous section, which also includes general facts that are independent of the material, we will now present similar results for the Ag particles. To begin with, results from the arrays having 200 nm lattice constants and 20 nm thick Ag nanodisks with growing size are shown in figure 5.17.

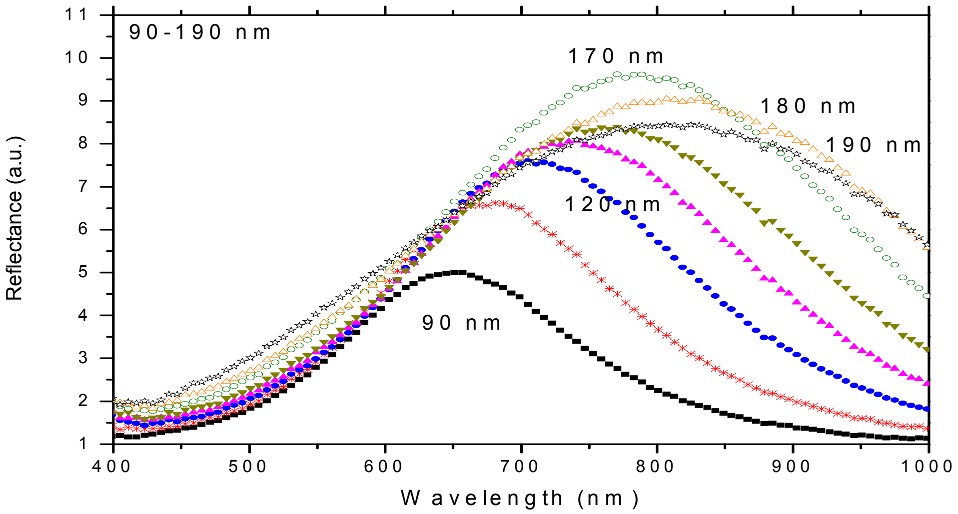

Figure 5.17: Reflectance spectra of Ag nanoparticle arrays located on ITO coated glass with a lattice constant of 200 nm. Diameters of the nanodisks vary from 90 to 190 nm.

Similar to the case of Au, 200 nm separation between the neighboring particles is short enough for strong coupling. Peaks are broadened due to coupling and no polarization dependent peaks can be distinguished. Furthermore; in the case of higher exposure doses; particles are in contact with each other, degrading the peak value and broadening the bandwidth. Such a situation is just like the case illustrated in figure 3.5 where a 60 nm Ag cylinder was located in a conductive host. Although a very similar case is already observed for Au nanoparticles, current example can give more information, since the particles are not completely in touch. Given with up-triangles in figure 5.17, nanodisks with diameter of about 180 nm are observed to have a slightly lower peak value when compared to the smaller nanoparticles given with open-circles. Also, the peak is clearly broadened tending to keep the area under curve constant. On the other hand, as the particle sizes are increased to values around 190 nm, peak value continues to decrease but no more broadening can be observed. Being represented with open-stars in figure 5.17, it is clear that resonance peak is about to diminish in intensity due to the extensive broadening in this sample. Figure 5.18 gives the SEM images of those two Ag nanodisk arrays.

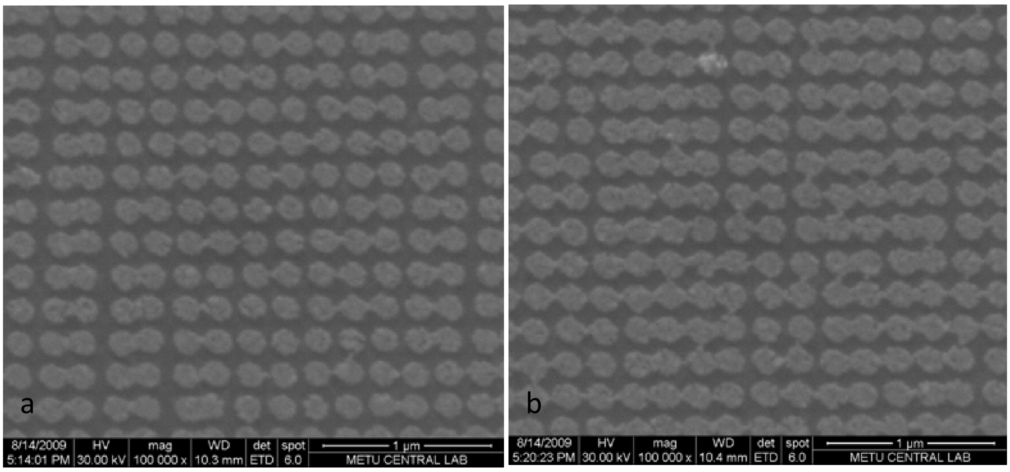

Figure 5.18: SEM images of Ag nanoparticles with diameters of approximately 180 and 190 nm.

SEM images of arrays clarify the contact between the neighboring particles. In figure 5.18a, disks with diameter around 180 nm are found to be in contact only with single neighbors and forming pairs of nanoparticles. This situation can be simplified as an ellipsoid with an aspect ratio of 2, except from the fact that there is a ‘bridge’ between two lobes limiting the path of oscillating electrons. Slight decrease in the intensity can be attributed to this fact while broadening of the peak can be explained with the larger dimensions of the resulting pairs.

However, for sample given in figure 5.18b, up to ten particles can be found to be in contact forming a large cluster of Ag disks. In this case, talking about localized surface plasmons becomes much difficult. For doses slightly larger than the latter example, the resulting pattern can be expected to behave like a mirror as in the case of Au nanoparticles given in figure 5.13.

Comparison of Ag and Au nanoparticles with similar parameters experimentally, leads to disappointing results. Promising predictions by use of simulations on Ag nanoparticles are found to be misleading. Figure 5.19 gives the reflectance spectra of both metals with the same parameters.

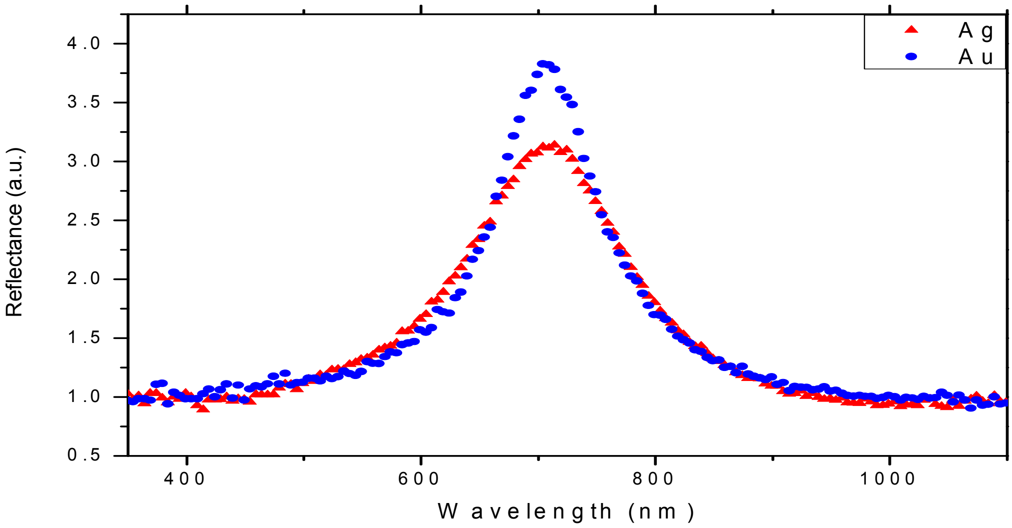

Figure 5.19: Reflectance spectra of Au and Ag nanoparticle arrays having the same parameters.

To avoid any error due to the geometries of the particles, reflectance data taken with polarized light from axes with the same length are considered. Referring to the simulations carried out through this study, figures 2.7 and 5.16, it is expected that Ag nanoparticles should provide higher peak values at relatively shorter wavelengths when compared to Au. Many experimental studies employ Ag nanoparticles because of this expectation [66]. However, experimental findings are in conflict with the theoretical predictions. In practice, Au nanoparticles are observed to have higher reflectance peak. Also, positions of the peaks are found to be the same for both metals.

The important fact altering the efficiency of Ag is the oxidation of the metal. Ag is known to be easily oxidized while Au is well known with less oxidation. Since the optical experiments are performed at most 15 hours after the production of samples, the oxidation can be thought to be responsible for the decrease in the peak intensity of reflectance from Ag particles. Of course, this possibility should be checked experimentally which is a straightforward procedure. Figure 5.20 gives the reflectance spectra of Au and Ag nanoparticles taken as a function of time to see the effect of oxidation on both metals.

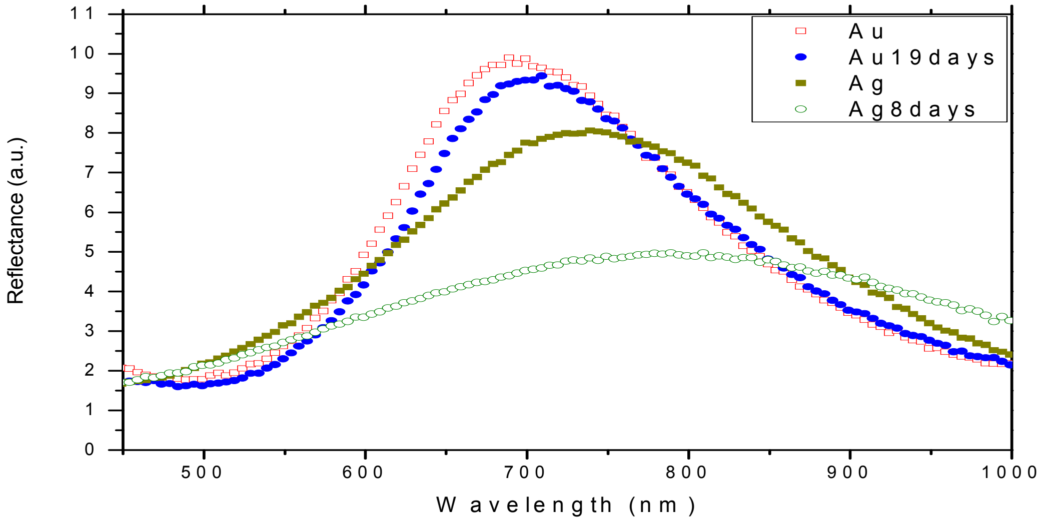

Figure 5.20: Reflectance spectra of Au and Ag nanoparticles measured multiple times.

As expected; resonance peak of Au nanoparticles measured 19 days after the production is almost the same as the one measured on the day of production. The slight difference can be attributed to little amount of oxidation which might occur on the Au surface. However, reflectance peak of Ag nanoparticle array is highly degraded and broadened only in 8 days. The resonance behavior is almost lost. Considering the fact that oxidation rate is expected to be larger at the beginning, it can be concluded that all optical measurements of Ag samples are affected once they are relocated outside the evaporation chamber. The degradation of the peak can be explained by the reduction in the free electron density in the metal which directly affects the optical efficiency. Thus, the inconsistency of the simulations with experimental data can be attributed to the oxidation of silver nanoparticles. The oxidation effect can be observed with naked eye for arrays with sufficiently large area, 200x200 μm^2. Yellow color of the Ag array turns to grey which is the characteristic color of oxidized silver when reflected light is observed. Also, SEM images of Ag nanoparticles verify the oxidation process. SEM image of Ag nanodisks 30 days after the production date can be seen in figure 5.21.

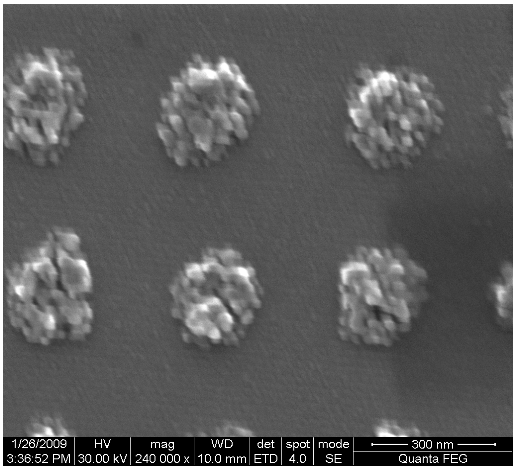

Figure 5.21: SEM image of Ag nanoparticles 30 days after the date of production.

When compared with the previous SEM images of Ag and Au nanoparticles, deformation of the shape of the sample due to oxidation can be noticed easily. Both the reduction in the number of free electrons and relative change in the dielectric constant of the surrounding medium are responsible for the decrease and red shift in the resonance peak for silver nanoparticles.

In the previous section, where spectral data of Au nanoparticle are discussed, patterns were consisting of ellipsoidal elements. For the sake of clarity, disks having geometries closer to circles will be considered also. Figure 5.22 shows both polarization components and effects of lattice constant on the resonance for Ag nanoparticle arrays. Red shift of the resonance peak can be seen for the case of Ag arrays clearly for both polarized and unpolarized illumination, which is similar to the Au particles presented in the previous section. Being different than the Au nanoparticles, peak values for polarized illumination are found to be much closer to each other. This is obviously due to the geometry of the metal nanoparticles. If polarization independent peaks are required, it is possible to achieve this to a high degree by producing nanodisks with cylindrical symmetry. In our case, time limitations had priority leading to high exposure rates which, in turn, result in asymmetrical particles due to the reasons already discussed in chapter 4.

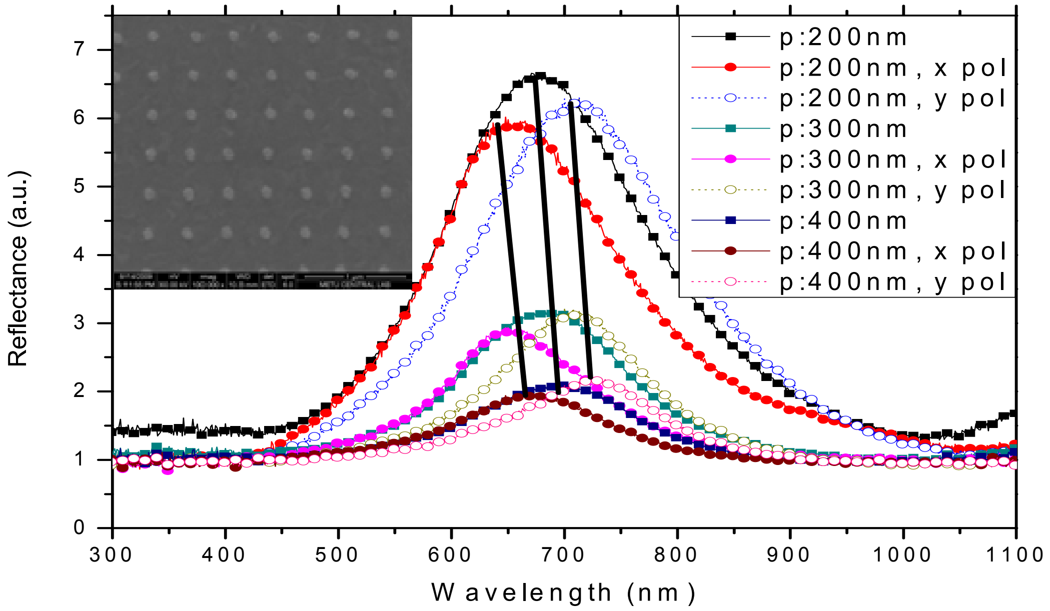

Figure 5.22: Reflectance of Ag nanoparticle arrays with different lattice constants. Polarized components of the peaks are also given. Inset presents the SEM image of corresponding Ag nanoparticles.

SEM image of corresponding nanoparticles verifies the uniformity of samples being discussed. Slight deviations in the symmetry of the disks are directly perceived in the resonance behavior of the arrays under linearly polarized incoming light.

One of the most effective parameters on the resonance condition of metal nanoparticles is the dielectric constant of the surrounding medium as discussed earlier in chapter 2 and 3 in this study. In figure 3.5, DDA simulation for a Ag disk in water is considered and resulting peak is found to shift to longer wavelengths. Figure 5.23 provides the experimental verification of a similar behavior where particle array is coated with PMMA to obtain a larger dielectric constant of surrounding medium. Having refractive index of 1.49 approximately in the visible region and very low extinction, PMMA is suitable for reflectance measurements. Also, uniform coating of a thin layer of 100 nm by spin coating method is possible and durability is ensured once PMMA is dried. Reflectance spectra of Ag nanoparticles before and after PMMA coating are given in figure 5.23.

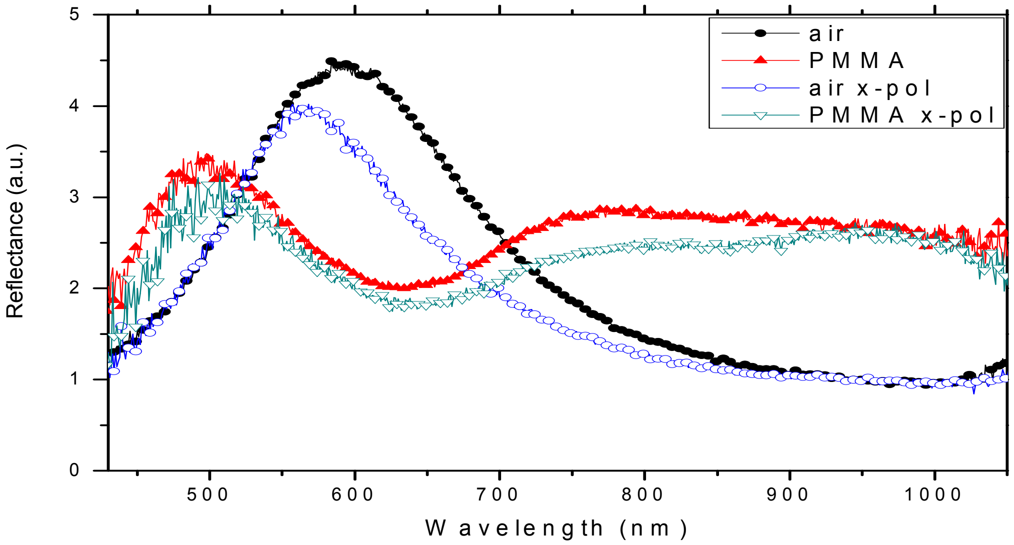

Figure 5.23: Reflectance spectra of Ag nanoparticle arrays w/o PMMA coating.

Reflectance spectrum obtained from the sample without PMMA layer indicates that the nanoparticles in the array are ellipsoidal disks with axes of approximately 70-80 nm. Considering other spectra obtained for Ag, presented previously, those dimensions are reasonable. One of the polarization components is included in the graph to present the asymmetrical nature of the particles. When the PMMA layer is coated on the surface and the dielectric constant of the medium is increased, a red shift in the resonance peak is observed. However, the intensity of the peak is reduced strongly. This is, most probably, due to the fact that scattered light form the particles gain some angle and reflect back at the PMMA-air interface. Thus, intensity of the signal reaching the detector decreases. Another important outcome of this data is the additional peak occurred at about 480 nm. Since the dipole emission from the nanoparticles are observed to be red shifted, the peak at the shorter wavelengths is, obviously, due to the quadrupole terms. Since the data given in figure 3.5 for the case of Ag particle in water is very similar to this situation, no more simulation data will be presented for this sample. However, the quadrupole term becomes apparent in the water environment when compared to the vacuum case, and similar behavior should be expected for PMMA coating.

At the very beginning of this study, it is mentioned that particles being capable of scattering the incident light in to the host material to increase absorption are of interest. Also, as presented in figure 2.6, it is shown that the tendency of the particle to absorb or scatter the illuminating light is related to the size of the target. For silver nanoparticles, the critical diameter where the scattering becomes dominant is calculated from the quasistatic approximation to be around 70 nm. To present the absorption and scattering characteristics of Ag particles below and above this value, nanodisks with diameters of 50 and 80 nm are studied. Since ITO layer coated on the surface of the microscope slide to prevent charging is found to be affecting reflectance intensities, it will be healthier to consider arrays patterned on bare glass. Reflectance data of those particles are presented in figure 5.24.

Due to the absence of ITO layer on the surface, reflectance intensity is lower than the previous examples of Ag nanoparticles with sizes around 80 nm. However, peak value is almost at the same wavelengths. These results are in agreement with the deductions made from the data presented in figure 5.3 in this chapter. In addition, Ag nanoparticles with the smallest size (50 nm) provided us the shortest resonance wavelength. It should be noted here that, although resonance of Ag and Au nanoparticles were found to be at very similar positions in previous examples where relatively larger peak positions were obtained, it would not be possible to observe a resonance peak for Au nanoparticles below 520 nm which is the plasma wavelength for this metal.

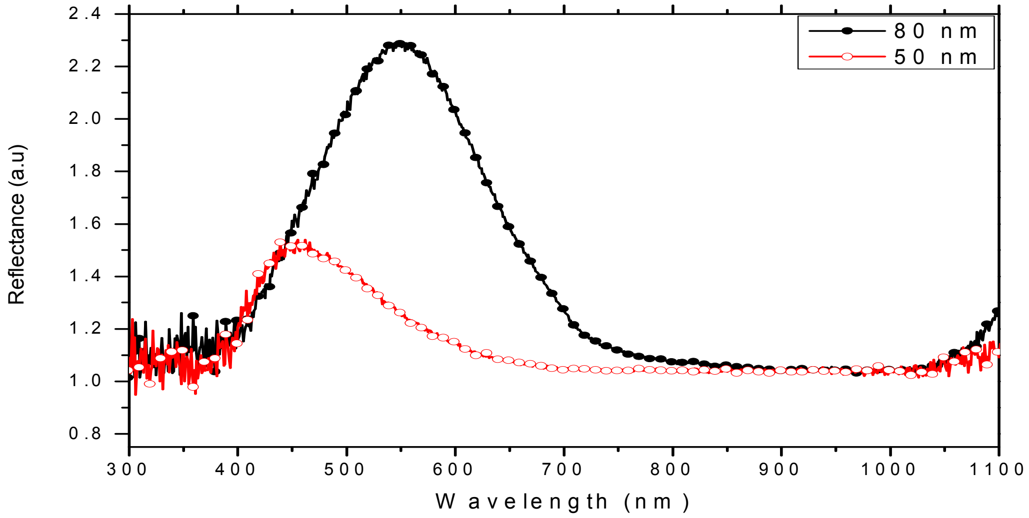

Figure 5.24: Reflectance spectra of Ag nanodisks with diameters of 50 and 80 nm.

It is not surprising to expect a larger peak value for 80 nm sized particles when previous discussions on the effect of increasing size on the particle-light interaction due to the increasing metal content are considered. To explore the effect of size on the absorption and scattering cross sections, pictures taken with optical microscope in both reflection and transmission mode can be examined. Figure 5.25 gives the images of Ag arrays patterned on bare glass consisting of 50 and 80 nm sized nanodisks.

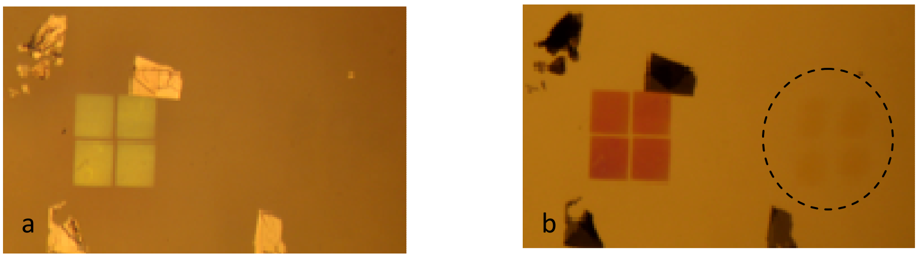

Figure 5.25: Reflection (a) and transmission (b) through Ag nanoparticles with diameters of 50 (right) and 80 (left) nm.

It is clear from the images that the color of the array is affected by the reflectance peak positions. Covering the region between 450-600 nm and having the peak value at around 540 nm, the 80 nm Ag array has a greenish yellow appearance while 50 nm Ag particles cannot be noticed due to the low scattering cross section. However, when the transmitted light is examined, both arrays can be observed. Of course, 80 nm particles provide better contrast due to the larger dimensions. 50 nm particles, on the other hand, can be noticed with background illumination but cannot be observed with front illumination. One can deduce from this fact that 50 nm Ag nanodisks have tendency to absorb the light rather than scattering back into the medium.

In addition to the images, reflectance and transmittance data of a certain group of samples should be compared to obtain reliable conclusions. Figure 5.26 provides the reflectance and transmittance measurements of nanoparticle arrays with sizes varying from 60 to 130 nm.

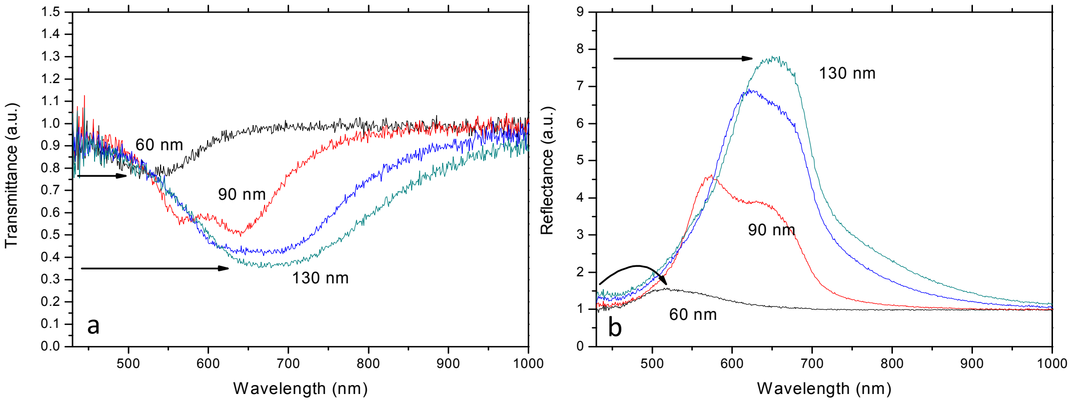

Figure 5.26: Transmittance and reflectance of Ag nanoparticles with varying size. Peak ratio of 60 and 130 nm particles in two data are found to be different.

Comparing the peak ratios of 60 and 130 nm Ag particles for both transmittance and reflectance measurements, one can see that the ratio in transmittance intensity is 0.385 (0.25/0.65) while reflectance intensity is 0.194 (1.5/7.75). It is clear from the data presented in figure 5.26 that absorption efficiency of 60 nm particle dominates the scattering efficiency being in contrast with the 130 nm particle case.

Catering to the human eye directly, sometimes, microscope images provide better understanding of the nature of the problem when compared to SEM images or spectral data. Discussion on the cross sections can be extended by use of additional photos of metal nanoparticles taken with optical microscope. Image of an Ag particle array with different lattice constants on perpendicular axes, taken under front illumination, is given in figure 5.27.

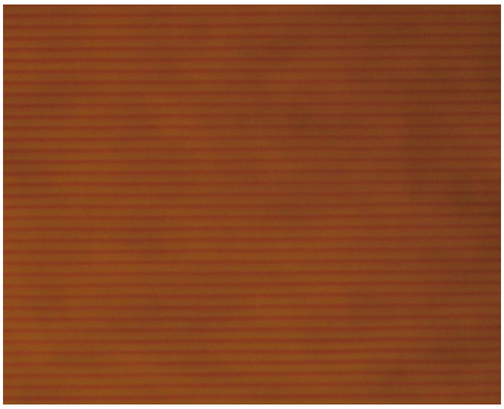

Figure 5.27: Image of an Ag nanopartcile array taken under front illumination with optical microscope. Lattice constants of the array are 200 and 1000 nm in perpendicular axes.

With front illumination, image taken with optical microscope provides information on the scattering cross section of the nanoparticles. Considering the size of the metal nanoparticles which are around 100 nm, one cannot expect to see the particles with eye even by use of an optical microscope due to the diffraction limits. However, in the case of Ag particles, chains of nanodisks can be resolved in the vertical axis where the lattice constant is 1000 nm. Obviously, the reason for this result is the enhanced scattering cross section of the Ag nanodisks due to the LSPR. Yellow color of the nanoparticle chains are due to the resonance positions of particles.

After examining the resonance behavior spectrally with optical setups, one can gain insight to the mechanisms by making a revision on the images. Images of Ag nanoparticles with increasing sizes under front and back illumination are presented in figure 5.28. The size of the nanodisks decreases from right to left and the lattice constants increases from top to bottom. Nanoparticles with largest diameter are found to provide a bright yellow color for the case of front illumination. As the nanoparticle size decreases, the color shifts from yellow to green due to the blue shift in the resonance condition and the brightness is lost because of the low surface coverage of metal.

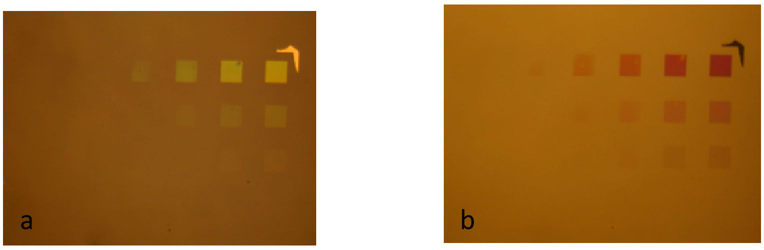

Figure 5.28: Images of Ag nanoparticle arrays with varying lattice parameters and particle diameters, taken through optical microscope under front (a) and back (b) illumination.

On the other hand, for the case of back illumination, appearances of the patterns are related to the extinction peaks. Excluding the scattered and absorbed portion of the illuminated light, the remained colors determine the appearance of arrays. Again, the contrast is lost as the particle size decreases or lattice constant increases. Notice the fifth nanoparticle array from the right in the uppermost row. It cannot be distinguished from the background in the front illumination case while it can be seen with a careful look in the back illumination mode, supporting the discussions made about the dominance of absorption cross section for smaller nanoparticles.

Finally; optical images of nanoparticle arrays, presented in figure 5.28, under back illumination before liftoff process is presented in figure 5.29. Apart from metal nanoparticles, a thin Ag film with periodically ordered nanoholes also exists in the system. Distance between the disks and the holes are approximately 100 nm which is the thickness of the PMMA layer which is not removed yet.

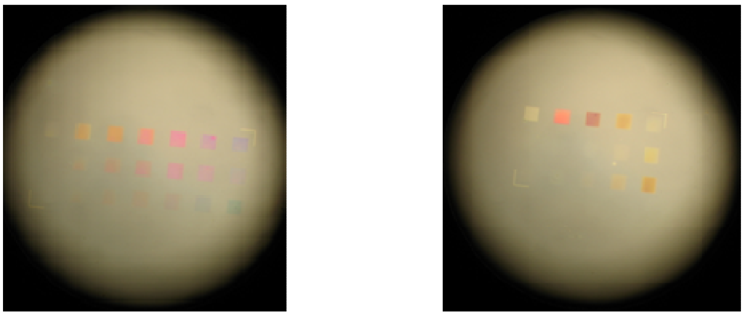

Figure 5.29: Images of Ag nanoparticles standing behind a thin Ag film with periodically ordered nanoholes under back illumination.

Having the same sizes and material with the previous example of Ag nanoparticles, these samples give us the chance to comment on the mechanism taking place. Strong contrast and color change within the rows can easily be observed in figure 5.29. It is obvious both from the reflectance spectra and images considered in this study that, obtaining distinct colors of that kind is not possible by use of nanoparticle arrays only. It can be suggested that transmittance bands of both nanoparticles and nanoholes overlap and allow a narrower band of incident light to transmit. Thus, diverse colors seen in figure 5.29 are obtained. Being a combination of two systems, nanoholes and particles, and providing promising transmittance; this issue can be considered as a research area on its own.

CHAPTER 6

CONCLUSIONS

In this work; optical properties of metal nanoparticles, fabricated by electron beam lithography which is a slow but well controllable technique, are studied both theoretically and experimentally. Au and Ag were chosen due to their endurance and low absorption efficiencies, respectively. A microscope based setup is designed to perform efficient reflectance and transmittance measurements on the nanoparticle arrays which are patterned on small areas, 100x100 μm^2, because of the uniformity issues. A computer code based on the Discrete Dipole Approximation method is written and employed to simulate the systems studied experimentally.

Self assembly growth technique is also used to fabricate metal nanoparticles on glass substrate, enabling us to make a comparison with EBL. Size variations and their effect on the resonance conditions are discussed and uniformity of the samples fabricated with EBL is verified.

Exposure doses needed to pattern desired geometries on samples with different conductivities are determined. Also, it is shown that the amount of beam current plays crucial role on the dimensions of nanoparticles and minimum achievable sizes. Also, the lattice constants of the arrays are found to influence the size of the nanoparticles due to the proximity effect. For relatively closer particles, the same parameters of exposure are shown to lead to features with larger dimensions. Furthermore, it is proposed that exposures with higher beam currents and shorter dwell times result in deformed geometries because of the astigmatism of the system while low beam currents and large dwell times reduce the asymmetries since dose on the exposed region is averaged over time. Thin Au film is used as the antistatic layer to solve the charging problem for insulating substrates which is not a widely preferred method for the case of processes employing PMMA. The challenges occurring during the development of the samples are attributed to the turbidity of PMMA in ternary systems involving water and MIBK. Heat treatment of the sample is found to solve the problem by removing the residuals on the sample due to additional steps of removing thin Au layer. Although feature sizes down to 40 nm are obtained, mostly particles with diameters larger than 80 nm are studied because of the dominance of scattering efficiency on these dimensions.

Effects of the thin ITO layer deposited on the glass substrates to simplify e-beam patterning are examined and reflectance intensities on the resonance regions are found to be much higher than the samples patterned on bare glass. Additional boundary between ITO film and glass is believed to be responsible for this increase since the light scattered from the nanoparticle array is expected to gain an angle of incidence due to the dipole emissions. However, expected red shift of the resonance peak due to the higher dielectric constant of ITO in visible region could not be observed experimentally. It is concluded that the difference between the optical constants of glass and ITO is not large enough to change the effective dielectric constant of the two layered system such that shifts on the resonance peak over brims the margin of error due to size deviations of particles in the illuminated array.

Data from reflectance measurements are used to examine the resonance conditions of metal nanoparticles and extinction efficiencies obtained for the samples simulated with DDA are found to be almost in agreement with experimental results. Ellipsoidal Au particles produced with high beam currents and short dwell times are found to have two separate reflectance peaks which can be resolved by use of polarized illumination. Increase in the particle size is found to result in red shift of the peak position and broader bandwidths due to higher order resonances. Peak intensities increased for larger dimensions for constant periods due to higher surface coverage. However, for particle sizes close to the lattice constant of the array, resonance peaks diminished in intensity since the plasmons are no more localized due to the contacts between particles. The main effect of the lattice constants of the arrays is found to be a reduction and slight red shift in the peak intensity. Reduced intensity is attributed to the lower metal content in the particle. Furthermore, increasing thickness of the particles is found to result in a blue shift and larger peak intensity which is again related to the metal content. One of the most effective parameters on the resonance peak is observed to be the dielectric constant of the surrounding medium. Coating a 100 nm thick PMMA layer over the nanoparticle arrays resulted in a significant shift and broadening in the peak and occurrence of higher order resonance peaks in shorter wavelengths.

Superior optical properties of Ag nanoparticles are found to be degraded due to the oxidation problem. Although exact and numerical calculations on the extinction efficiencies of Ag nanoparticles yielded promising results, reflectance measurements showed that efficiencies obtained from Ag particles cannot exceed the values obtained from Au nanoparticles. Multiple experiments on both Au and Ag nanoparticles showed that peak intensities of Au samples stay almost the same even for measurements performed 19 days later while Ag peaks are observed to diminish within a week. This is obviously a result of Ag oxidation as described above.

Dominance of absorption in particles with relatively small dimensions is verified from the images of arrays consisting of different feature sizes taken under back and front illumination in microscope based setup. Also, enhancement in the cross sections of nanosized particles is observed from the optical microscope images. Although the features have dimensions smaller than the diffraction limits, chains of metal nanoparticles are found to be recognizable with optical microscope. This phenomenon is attributed to the enhanced extinction cross sections of the metal nanoparticles in the array. Also, systems consisting of periodically ordered, nano sized particles and holes with varying dimensions are shown to provide diverse colors which can be considered as a promising tool for applications such as display technologies.

Being well predictable and controllable, localized surface plasmon resonances are found to be promising for applications such as absorption and emission enhancement as well as optical modulation. Further studies will be conducted on the adaptability of this phenomenon to absorption based optoelectronic devices such as solar cells with various physical structures as well as optical modulators.

REFERENCES

[1] Faraday M.; Phil. Trans. R. Soc. Lond., 147, 145 (1857).

[2] Garnett J. C. M.; Phil. Trans. R. Soc. Lond., 203, 385 (1904).

[3] Mie G.; Ann. Phys., 25, 377 (1908).

[4] Yee K. S.; IEEE Trans. Antennas Propag., 14, 302 (1966).

[5] Purcell E. M., Pennypacker C. R.; Astrophys. J., 186, 705 (1973).

[6] Zia R., Schuller J. A., Chandran A., Brongersma M. L.; Mat. Tod.; 9, 20 (2006).

[7] Homola J.; Springer Ser. Chem. Sens. Biosens.; 4, 33 (2006).

[8] Stuart H. R., Hall D. G.; Appl. Ohys. Lett.; 73, 3815 (1998).

[9] Schadt D. M., Feng B., Yu E. T.; Appl. Phys. Lett.; 86, 063106 (2005).

[10] Derkacs D., Lim S. H., Matheu P., Mar W., Yu E. T.; Appl. Phys. Lett.; 89, 093103 (2006).

[11] Nakayama K., Tanabe K., Atwater H. A.; Proc. SPIE; 7047, 704708 (2008).

[12] Pradhan A. K., Konda R. B., Mustafa H., Mundle R., Bamiduro O. Roy U. N., Cui Y., Burger A.; Optics Express; 16, 6202 (2008).

[13] Hagglund C., Zach M., Kasemo B.; Appl. Phys. Lett.; 92, 013113 (2008).

[14] Catchpole K. R., Pillai S.; J. Appl. Phys.; 100, 044504 (2006).

[15] Catchpole K. R., Pillai S.; J. Luminescence; 121, 315 (2006).

[16] Catchpole K. R.; Phil. Trans. R. Soc. A; 364, 3493 (2006).

[17] Pillai S., Catchpole K. R., Trupke T. Green M. A.; J. Appl. Phys.; 101, 093105 (2007).

[18] Beck F. J., Polman A., Catchpole K. R.; J. Appl. Phys.; 105, 114310 (2009).

[19] Biteen J. S., Pacifici D., Lewis N. S., Atwater H. A.; Nano Letters; 5, 1768 (2005).

[20] Fukushima M., Managaki N., Fujii M. Yanagi H. Hayashi S.; J. Appl. Phys.; 98, 024316 (2005).

[21] Mertens H., Polman A.; Appl. Phys. Lett.; 89, 211107 (2006).

[22] Tanabe K.; Materials Letters; 61, 4573 (2007).

[23] Garcia H., Kalyanaraman R., Trice J., Sureshkumar R.; Phys. Review B; 75, 045439 (2007).

[24] Kottman J. P., Martin O. J. F., Smith D. R., Schultz S.; New J. Phys.; 2, 27 (2000).

[25] Kalele A. A., Tiwari N. R., Gosawi S. W., Kulkarni S. K.; J. Nanophotonics; 1, 012501 (2007).

[26] Lal S., Link S., Halas N. J.; Nature Photonics; 1, 641 (2007).

[27] Teperik T. V., Abajo F. J. G., Borisov A. G., Abdelsalam M., Bartlett P. N., Sugawara Y., Baumberg J. J.; Nature Photonics; 2, 299 (2008).

[28] Yu E. T., Derkacs D., Lim S. H., Matheu P., Schaadt D. M.; Proc. SPIE; 7033, (2008).

[29] Jackson J. D.; Classical Electrodynamics; p.157 (1998).

[30] Novotny L., Hecht B.; Principles of Nano-Optics; p.398 (2006).

[31] Drachev V. P., Chettiar U. K., Kildishev A. V., Yuan H. K., Cai W., Shalaev V. M.; Optics Express, 16, 1186 (2008).

[32] Maier A.; Plasmonics: Fundamentals and Applications; p.11 (2007).

[33] Johnson P. B., Christy R. W.; Physical Review B; 6, 4370 (1972).

[34] Xu Y.; Appl. Optics; 34, 4573 (1995).

[35] Zhao J., Pinchuk A. O., McMahon J. M., Li S., Ausman L. K., Atkinson A. L., Schatz G. C.; Accounts of Chem. Research; 41, 1710 (2008).

[36] Kelly K. L., Coronado E., Zhao L. L., Schatz G. C.; J. Phys. Chem. B; 107, 668 (2003).

[37] Chien W. Y., Szkopek T.; Optics Express; 16, 1820 (2008).

[38] Bohren C. F.; Huffman D. R.; Absorption and Scattering of Light by Small Particles; p.83 (2004).

[39] Draine B. T.; Astrophys. J.; 333, 848 (1988).

[40] Draine B. T., Flatau P. J.; J. Opt. Soc. Am. A; 11, 4 (1994).

[41] Draine B. T., Goodman J.; Astrophys. J.; 405, 685 (1993).

[42] Biteen J. S., Sweatlock L. A., Mertens H., Lewis N. S., Polman A., Atwater H. A.; J. Phys. Chem. C; 111, 13372 (2007).

[43] Flatau P. J.; Optics Express; 12, 3149 (2004).

[44] Fan Z. H., Wang D. X., Chen R. S., Yung E. K. N.; Microwave and Opt. Tech. Lett.; 48, 1741 (2006).

[45] Taleb A., Petit C., Pileni M. P.; J. Phys. Chem. B; 102, 2214 (1998).

[46] Zhou X., Knoll W., Liu K. Y., Tse M. S., Oh S. R., Zhang N.; J. of Nanophotonics; 2, 023502 (2008).

[47] Ma F., Hong M. H., Tan L. S.; Appl. Phys. A; 93, 907 (2008).

[48] Wenzel T., Bosbach J., Stietz F., Trager F.; Surface Sci.; 432, 257 (1999).

[49] Daruka I., Barabasi A. L.; Phys. Rev. Lett.; 79, 3708 (1997).

[50] Ouacha H., Hendrich C., Hubenthal F., Trager F.; Appl. Phys. B; 81, 663 (2005).

[51] Trice J., Thomas D., Favazza C., Sureshkumar R., Kalyanaraman R.; Phys. Review B; 75, 235439 (2007).

[52] Hawes E. A., Hastings J. T., Crofcheck C., Mengüç M. P.; J. Quant. Spec. Rad. Trans.; 104, 199 (2007).

[53] Gotschy W., Vonmetz K., Leitner A., Aussenegg F. R.; Appl. Phys. B; 63, 381 (1996).

[54] Hicks E. M., Gunnarsson L., Rindevicius T., Zou S., Kasemo B., Kall M., Schatz G. C., Spears K. G., Duyne R. P.; Mater. Res. Soc. Symp. Proc.; 872 (2005).

[55] Hohenau A., Ditlbacher H., Lamprecht B., Krenn J. R., Leitner A., Aussenegg F. R.; Microelectronic Engineering; 83, 1464 (2006).

[56] Yokota Y., Ueno K., Mizeikis V., Juodkazis S., Sasaki K., Misawa H.; J. of Nanophotonics, 1, 011594 (2007).

[57] Lai J. Y., Lin S. F., Lin F. C., Wang D. M.; J. Poly. Sci. B; 36, 607 (1998).

[58] Nammalvar V., Wang A. Drezek R.; J. of Nanophotonics; 1, 013510 (2007).

[59] Lin A., Han W. T.; J.of Nanophotonics, 1, 013554 (2007).

[60] Aslan M. M., Mengüç M. P., Videen G.; J. Quant. Spec. Rad. Trans.; 93, 207 (2005).

[61] Francoeur M., Venkata P. G., Mengüç M. P.; J. Quant. Spec. Rad. Trans.; 106, 44 (2007).

[62] Link S., El-Sayed M.; J. Phys. Chem. B; 103, 8410 (1999).

[63] Shalaev V. M., Kawata S.; Nanophotonics with Surface Plasmons, p.141 (2007).

[64] Bakker M. R., Drachev V. P., Liu Z., Yuan H. K., Pedersen R. H., Boltasseva A., Chen J., Irudayaraj J., Kildishev A. V., Shalaev V. M.; New J. Phys.; 10, 125022 (2008).

[65] Zou S., Schatz G. C.; J. Chem. Phys.; 121, 12606 (2004).

[66] Biteen J. S., Lewis N. S., Atwater H. A., Mertens H., Polman A.; Appl. Phys. Lett.; 88, 131109 (2006).